Earth Syst. Sci. Data, 16, 2831–2855, 2024
https://doi.org/10.5194/essd-16-2831-2024

Open Access Earth System Science Data

A Level 3 monthly gridded ice cloud dataset derived from 12 years of CALIOP measurements

David Winker[1], Xia Cai[1], Mark Vaughan[1], Anne Garnier[2,1], Brian Magill[2,1], Melody Avery[1], and Brian Getzewich[1]

[1]NASA Langley Research Center, Hampton, Virginia 23681, USA
[2]Analytical Mechanics Associates, Hampton, Virginia 23666, USA

Correspondence: David Winker (david.winker@nasa.gov)

Received: 2 October 2023 – Discussion started: 20 November 2023
Revised: 14 March 2024 – Accepted: 28 March 2024 – Published: 19 June 2024

Abstract. Clouds play important roles in weather, climate, and the global water cycle. The Cloud-Aerosol Lidar with Orthogonal Polarization (CALIOP) onboard the Cloud-Aerosol Lidar and Infrared Pathfinder Satellite Observation (CALIPSO) spacecraft has measured global vertical profiles of clouds and aerosols in the Earth's atmosphere since June 2006. CALIOP provides vertically resolved information on cloud occurrence, thermodynamic phase, and properties. We describe version 1.0 of a monthly gridded ice cloud product derived from over 12 years of global, near-continuous CALIOP measurements. The primary contents are monthly vertically resolved histograms of ice cloud extinction coefficient and ice water content (IWC) retrievals. The CALIOP Level 3 Ice Cloud product is built from the CALIOP Version 4.20 Level 2 5 km Cloud Profile product that, relative to previous versions, features substantial improvements due to more accurate lidar backscatter calibration, better extinction coefficient retrievals, and a temperature-sensitive parameterization of IWC. The gridded ice cloud data are reported as histograms, which provides data users with the flexibility to compare CALIOP's retrieved ice cloud properties with those from other instruments with different measurement sensitivities or retrieval capabilities. It is also convenient to aggregate monthly histograms for seasonal, annual, or decadal trend and climate analyses. This CALIOP gridded ice cloud product provides a unique characterization of the global and regional vertical distributions of optically thin ice clouds and deep convection cloud tops, and it should provide significant value for cloud research and model evaluation. A DOI has been issued for the product: https://doi.org/10.5067/CALIOP/CALIPSO/L3_ICE_CLOUD-STANDARD-V1-00 (Winker et al., 2018).

1 Introduction

Covering a large fraction of the globe, atmospheric ice clouds have significant impacts on Earth's radiation budget and also play a key role in the atmospheric hydrologic cycle. Due to the cold temperatures at which ice clouds are found, they impact both longwave and shortwave radiation, with the net balance dependent on optical depth and other cloud properties (Berry and Mace, 2014; Hong et al., 2016). Deep convective clouds contain large quantities of ice but represent a very small fraction of global cloud cover (Sassen et al., 2009). Ice detrained from deep convection and in situ formation within moist layers in the upper troposphere are responsible for most of the global coverage of ice clouds. Most of this global coverage is optically thin, making a small contribution to the global ice mass budget but significant contributions to the radiation budget (Haladay and Stephens, 2009).

Satellite sensors are our only means of observing the global distribution of ice clouds and characterizing their properties. These global observations are essential for understanding the mean distribution of atmospheric ice and its variability. Accurate representation of ice clouds is important for both numerical weather prediction and climate modeling. Satellite observations are critical for assessing whether these models produce realistic simulations of atmospheric ice clouds, both for simulating a realistic energy balance and for properly modeling the hydrologic cycle. Indeed, Waliser

et al. (2009) pointed out that discrepancies between models are much larger for ice water path (IWP) and ice water content (IWC) than for parameters such as global mean cloud cover, for which there are better observational constraints. Intercomparison studies, however, persistently show a large spread in IWP between satellite datasets (Waliser et al., 2009; Eliasson et al., 2011; Duncan and Eriksson, 2018). Satellite datasets exhibit similar geographical patterns of ice distribution but there are large differences in the magnitude of IWP. These differences between observational datasets make it difficult to validate models and to identify avenues for improvement.

Global data on IWP have been available for decades from a number of passive visible and infrared (VIS/IR) satellite sensors and several passive microwave sensors (Buhl et al., 2017), but any one sensor is sensitive to only part of the IWP column (Eliasson et al., 2011; Waliser et al., 2009). VIS/IR sensors are only sensitive to thin clouds and the upper portions of deep clouds while nadir-viewing microwave sensors can retrieve ice through thick clouds but have trouble detecting thin ice clouds. These varying sensitivities are one reason for the large differences between satellite ice cloud datasets. Passive nadir-viewing sensors cannot measure the profile of IWC but only column IWP. Limb-viewing instruments such as the Microwave Limb Sounder (MLS) (Waters et al., 2006; Wu et al., 2008) and the Submillimeter Radiometer (SMR) on the Odin satellite (Murtagh et al., 2002) provide vertically resolved profiles of ice in the upper troposphere but have poor horizontal resolution, and interpretation of the measurements is complicated by the long tangent path through the atmosphere (Wu et al., 2009).

While passive imagers and radiometers provide detailed cloud mapping from space, a deeper and more comprehensive understanding of the spatial and temporal distributions of clouds on a global scale requires knowledge of cloud vertical distributions and multi-layer occurrence frequencies. New capabilities for retrieving vertically resolved IWC became available with the launch of the Cloud-Aerosol Lidar and Infrared Pathfinder (CALIPSO) (Winker et al., 2010) and CloudSat (Stephens et al., 2002) satellites in 2006. The Cloud-Aerosol Lidar with Orthogonal Polarization (CALIOP), the CALIPSO lidar (Hunt et al., 2009; Winker et al., 2009), operates at 532 and 1064 nm and has high sensitivity to optically thin ice clouds which are often undetected by the CloudSat W-band (94 GHz) profiling radar due to their small particle sizes (Mace et al., 2009). However, the CloudSat radar can penetrate optically thick clouds and all but the densest convective systems and therefore adds observations of dense ice clouds where CALIOP signals are completely attenuated.

Currently, perhaps the most complete observations of IWC throughout the vertical column come from two datasets that combine collocated data from CALIPSO and CloudSat: 2C-ICE (Deng et al., 2010) and DARDAR (Delanoë and Hogan, 2010). Noel et al. (2018) studied the representativity of the sun-synchronous observations from CALIOP relative to observations over the diurnal cycle from the CATS lidar. In some cases CALIOP observations represented extreme values of the diurnal cycle of cloud profiles, while taking CALIOP observations from both local overpass times (01:30 and 13:30) provided a good indication of the daily average cloud fraction profile, over both ocean and land. We have constructed a lidar-only Level 3 Ice Cloud product based on the CALIPSO Version 4.2 Level 2 Cloud Profile product which is more continuous, covering both day and night from June 2006 through December 2018. When data processing artifacts caused by intermittent low-energy laser pulses during the later years of the mission are resolved (Tackett et al., 2023), the product will be extended to cover the full CALIPSO mission. In addition to the more complete temporal coverage than the radar–lidar products, the dataset also benefits from using the latest versions of the CALIPSO cloud extinction and cloud thermodynamic phase algorithms (Young et al., 2018; Avery et al., 2020).

The primary contents of the CALIPSO Level 3 Ice Cloud product (hereafter, L3-ICE) are monthly statistics on ice cloud extinction and IWC. Results are reported on a uniform three-dimensional global grid of 2.5° longitude by 2.0° latitude and 120 m vertical resolution, from the sea-level surface to 20.2 km altitude. For each month, three data files are created. One reports statistics exclusively for daytime measurements; a second reports statistics exclusively for night-time measurements; and the third reports the combined day and night statistics.

Previous studies show that comparison of the mean values of the various satellite IWC datasets are difficult to interpret because instruments have different sensitivities and observe different portions of the IWP column (Waliser et al., 2009; Li et al., 2016). Intercomparison of histograms can be more meaningful and can identify differences in instrument sensitivities (Duncan and Eriksson, 2018). Therefore, L3-ICE profiles of ice cloud extinction and IWC are presented as gridded monthly histograms. The histograms are constructed using sample counts, rather than normalized frequency values, to allow proper aggregation of statistics to larger spatial and/or temporal scales.

The remainder of this paper provides a detailed introduction to the product, including the method of construction, quality control measures, characteristics of the data, and uncertainties. Section 2 discusses the CALIOP Level 2 5 km Cloud Profile product on which the L3-ICE is based. Section 3 describes the methods used to select high-confidence ice cloud extinction and IWC data and aggregate this Level 2 data onto a three-dimensional global grid. Section 4 presents a few results to illustrate product contents. Section 5 discusses sources of uncertainty (uncertainties due to sparse sampling, inability to probe deep convection, Level 2 cloud clearing). Section 6 assesses L3-ICE strengths and weaknesses via comparisons with the DARDAR and 2C-ICE

products. Finally, Sect. 7 presents a summary and a few thoughts on future development.

2 Input data

CALIOP is an elastic backscatter lidar transmitting linearly polarized laser pulses at 532 and 1064 nm. CALIOP is nadir viewing with a 90 m diameter receiver footprint every 335 m creating a curtain of profile observations along the satellite track. Backscattered light from the CALIOP laser is detected and sampled at high vertical resolution. The 532 nm receiver separately measures backscattered light polarized parallel and perpendicular to the polarization of the outgoing beam, allowing the identification of cloud thermodynamic phase (Hu, 2007). Below an altitude of 8.2 km, profiles are sampled at a vertical resolution of 30 m and every profile is downlinked. Between altitudes of 8.2 and 20.2 km, profiles are averaged onboard the satellite to 60 m vertical and 1 km horizontal resolution before being downlinked (Hunt et al., 2009). Details of radiometric calibration and other Level 1 processing are described in Powell et al. (2009), Kar et al. (2018), Getzewich et al. (2018), and Vaughan et al. (2019). Strongly scattering cloud and aerosol layers can be detected from single return profiles but averaging of multiple lidar shots is required to detect optically thin layers (Winker et al., 2009). Therefore, CALIOP Level 2 processing employs an iterative multi-scale averaging scheme to detect both weakly and strongly scattering layers at the highest practical horizontal resolution (Vaughan et al., 2009). This multi-scale averaging scheme results in a collection of atmospheric features detected at horizontal resolutions ranging from 1/3 to 80 km. Detected features are then classified as aerosol or cloud (Liu et al., 2019), and cloud layers are classified as liquid or ice. Ice layers are further classified as randomly oriented ice (ROI) or horizontally oriented ice (HOI) using differences in the backscatter and depolarization signatures of the layers (Avery et al., 2020).

L3-ICE is built from the Version 4.20 Level 2 Cloud Profile product (hereafter L2-CPro). L3-ICE uses L2-CPro altitude-resolved profiles of cloud properties, including 532 nm extinction coefficients and IWC, from the sea-level surface to 20.2 km altitude, which are reported at a vertical resolution of 60 m. Due to signal-to-noise ratio (SNR) limitations in the highest-resolution data, profiles of particulate extinction are only retrieved for clouds detected at horizontal averaging resolutions of 5, 20, and 80 km (Young and Vaughan, 2009; Young et al., 2018).

Profiles of IWC ($\mathrm{g\,m^{-3}}$) are derived from ice cloud extinction coefficients using a temperature-dependent parameterization based on in situ measurements acquired during a number of aircraft field campaigns conducted between 1991 and 2007 (Heymsfield et al., 2014; hereafter H14):

$$\mathrm{IWC}(z) = \left(\frac{\rho}{3}\right)\sigma(z)\alpha_T e^{\beta_T T(z)}, \quad (1)$$

Table 1. Temperature-dependent fitting parameters α_T and β_T used in Eq. (1).

Temperature (T), °C	α_T	β_T
$-56 < T < 0$	308.4	0.0152
$-71 < T < -56$	9.1774×10^4	0.117
$-85 < T < -71$	83.3	0.0184

where $\sigma(z)$ and $T(z)$ are the ice cloud extinction coefficient ($\mathrm{m^{-1}}$) and temperature (°C), respectively, at altitude z. The value adopted for the density of ice, ρ, is $0.91\,\mathrm{g\,cm^{-3}}$ (Heymsfield et al., 2014). The temperature-dependent fitting parameters α_T and β_T, given in Table 1, were determined from least-squares fitting of volume extinction coefficients and IWC directly measured in situ. Of several fits to the data explored in H14, Eq. (1) is the piece-wise fit that best reproduces the aircraft data across the full temperature range of −86 to 0 °C. The temperature dependence of the IWC vs. extinction relationship can be interpreted as due to a broadening of the particle size distribution as temperature increases (H14).

L3-ICE also uses ancillary data on atmospheric state and surface elevation that are contained in L2-CPro. Data describing the atmospheric state include temperature, pressure, relative humidity, and tropopause height, all taken from the NASA Global Modeling and Assimilation Office MERRA-2 product (Gelaro et al., 2017). Surface elevation data are taken from a digital elevation model (DEM) developed by the CloudSat team (Tanelli et al., 2014) which is primarily based on data from the NASA Shuttle Radar Topography Mission (SRTM) (NASA JPL, 2013), augmented by surface elevation data from GTOPO30, ASTER-GDEM, and NSIDC at high latitudes. Complete contents of the CALIOP layer and profile products are given in Vaughan et al. (2022).

3 Method

The L3-ICE is derived from the L2-CPro product in a series of steps involving data selection, quality screening, and construction of the histograms. Flags contained in L2-CPro are used to identify the locations of ice clouds within the profile. Quality screening is then applied to identify ice cloud layers which have high-confidence extinction retrievals. Finally, quality-screened monthly statistics are aggregated onto a global three-dimensional (3-D) grid, in the form of histograms of ice cloud extinction and IWC, along with various types of sample counts. Each of these steps is described in detail in the sections that follow.

3.1 Selection of ice cloud layers

Figure 1 outlines the decision tree used to select ice cloud data for inclusion in L3-ICE and steps in the process are il-

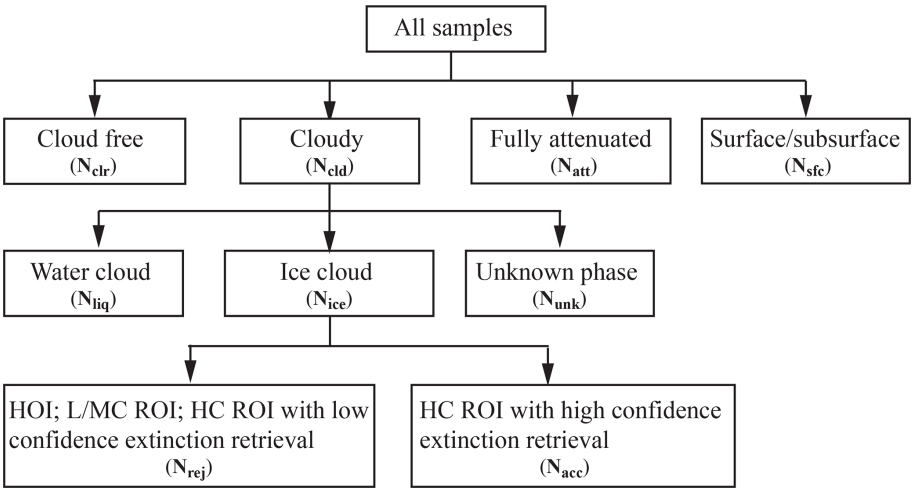

Figure 1. Decision tree for scene classification leading to selection of high-confidence ROI samples having high-confidence extinction retrievals (N_{acc}).

lustrated in Fig. 2. During this process several types of sample counts are accumulated and reported in L3-ICE (Table 2). The standard 532 nm attenuated backscatter browse image in Fig. 2a, in which Level 1 profiles are averaged to 5 km horizontal resolution, shows a scene dominated by optically thin ice clouds above an altitude of about 8 km. Clouds below 8 km are predominantly supercooled water and are mostly opaque to CALIOP. The *Atmospheric_Volume_Description* (AVD) parameter contains feature classification flags for each range bin in the L2-CPro profiles. The AVD contains flags identifying feature type and, for cloudy bins, the cloud type, cloud phase, and the level of confidence in the discrimination of cloud from aerosol and in the identification of cloud thermodynamic phase (Vaughan et al., 2022). As shown in Fig. 1, the first step of the Level 3 ice cloud selection process uses AVD flags to identify range bins, which are clear, cloudy, totally attenuated, contain the surface return, or are below the surface. Sample counts of each feature type are accumulated in the parameters N_{clr}, N_{cld}, N_{att}, and N_{sfc}, respectively. Range bins designated as "clear" are cloud-free but may contain aerosol.

Figure 2b illustrates the scene shown in Fig. 2a after feature classification. Black areas indicate the lidar signal has been completely extinguished by optically thick overlying clouds. The AVD also contains a quality assurance (QA) flag which indicates the confidence in the cloud–aerosol classification performed by the cloud–aerosol discrimination (CAD) algorithm (Liu et al., 2019). Cloudy range bins classified with high, middle, or low confidence are shown in light blue. Range bins classified as "No Confidence Cloud" are shown in red. A classification of "No Confidence" often indicates erroneous detection rather than a true cloud and these bins are rejected from further consideration.

Next, ice-water phase flags in the AVD are used to identify cloudy bins as ice clouds, liquid clouds, or "unknown phase" in cases where the ice-water phase algorithm was unable to classify the cloud phase. This happens most often when scattering from optically thin clouds is very weak or when very low in-layer SNR leads to contradictory results within the phase algorithm. These sample counts are accumulated, respectively, in the parameters N_{ice}, N_{liq}, and N_{unk}, where $N_{cld} = N_{ice} + N_{liq} + N_{unk}$. The AVD cloud phase flag further identifies whether the clouds are composed of randomly oriented ice (ROI) particles or horizontally oriented ice (HOI) particles. Figure 2c shows the classification of cloud phase in the example scene, separately showing the occurrence of ROI identified with high confidence (HC ROI, in white), with medium or low confidence (orange), HOI (gray), and liquid (blue). The phase flags show the upper layer is cirrus composed of ROI, classified with high confidence. Clouds located between 5 and 9 km altitude in this scene are mostly liquid clouds. Figure 2d shows the horizontal resolutions at which the cloud layers in Fig. 2c are detected. Most of the ice clouds are reported at 5 km horizontal resolution, with averaging over 20 km required to detect the optically thinner parts of the cirrus layer, while many of the water clouds are detected with single shots. The solid black line shows the altitude at which the overlying cloud optical depth (the cloud optical depth integrated from 20.2 km down to altitude z) reaches 2. Because substantial aerosol layers are only rarely lofted to cirrus altitudes, we ignore aerosol contributions in these optical depth calculations. When the column cloud optical depth is less than 2, the line drops to the surface. In this scene the optical depth 2 threshold is most often exceeded when a liquid cloud is encountered. The horizontal dashed line indicates the altitude of the freezing level, showing that most of the liquid clouds in this scene are supercooled. Note that in this scene there are no high-confidence ROI layers detected beneath liquid clouds.

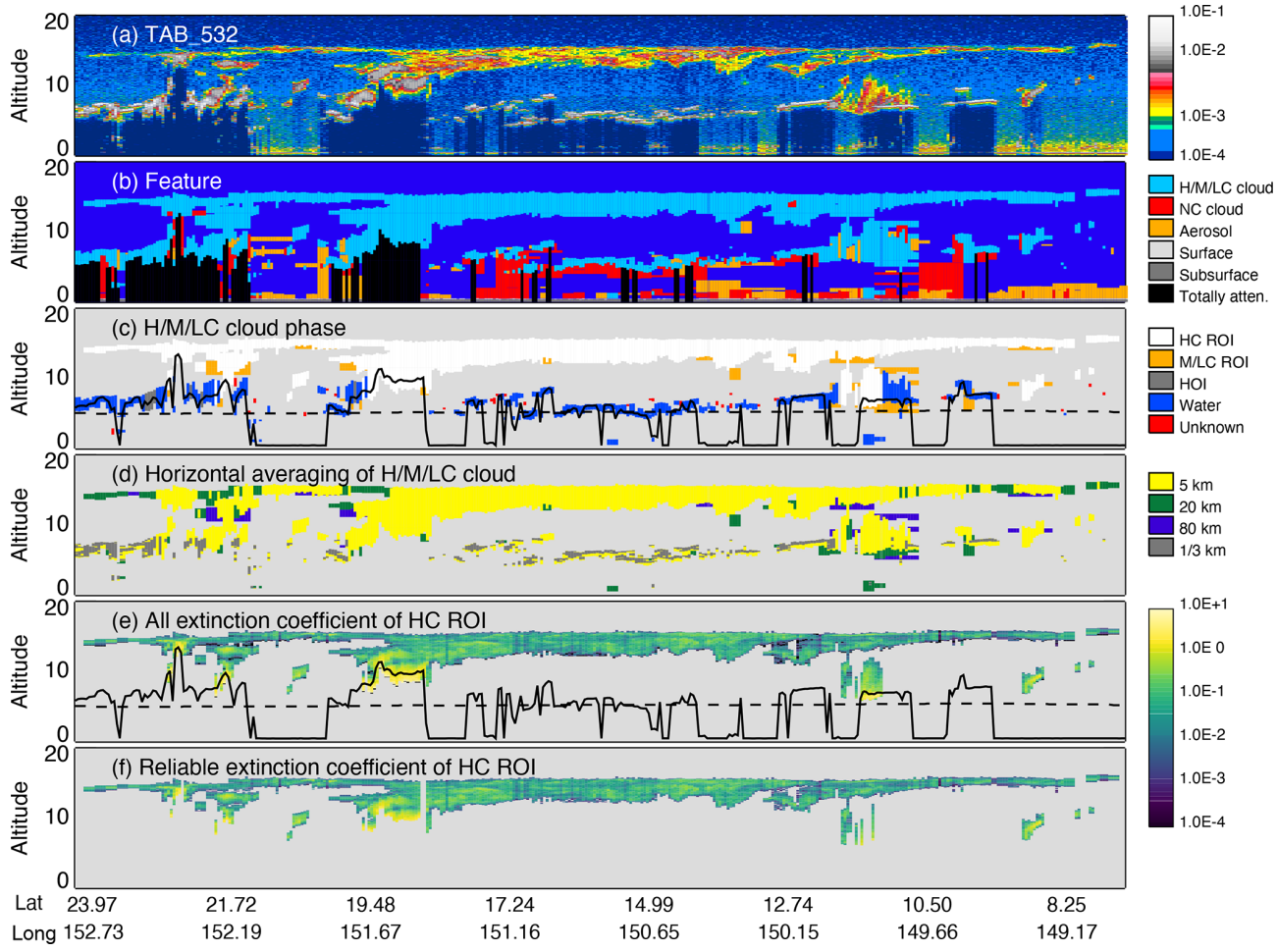

Figure 2. Illustration of the steps involved in the selection of high-confidence ice clouds and extinction values: **(a)** 532 nm attenuated backscatter profiles ($km^{-1}\,sr^{-1}$); **(b)** feature classifications; **(c)** cloud phase classifications; **(d)** horizontal averaging required to detect cloud layers; **(e)** profiles of all extinction coefficients (km^{-1}) retrieved within high-confidence ROI cloud layers; **(f)** extinction coefficient profiles after quality screening. Solid and dashed black lines in panels **(c)** and **(e)** show the altitude where the overlying optical depth reaches 2 and the freezing level, respectively. The scene is taken from granule 2008-07-28-T15-38-54ZN.

Table 2. Vertically resolved sample counts which are reported in the product.

Sample counts	Symbol
Surface or subsurface samples	N_{sfc}
Totally attenuated samples	N_{atten}
Cloud-free clear air samples	N_{clr}
Total cloud samples	N_{cld}
Liquid cloud samples	N_{liq}
Unknown phase cloud samples	N_{unk}
Total ice cloud samples	N_{ice}
Ice cloud samples, rejected	N_{rej}
Ice cloud samples, accepted	N_{acc}

3.2 Tests to ensure high-quality extinction retrievals

After range bins containing ice clouds are identified, several tests are applied to ensure that only range bins containing high-quality ice cloud extinction retrievals are selected for inclusion in the product. These screening steps are described below. Sample counts of ice cloud bins that pass all these screening tests are counted in *Ice_Cloud_Accepted_Samples* (N_{acc}), and samples which fail any of these tests are counted in *Ice_Cloud_Rejected_Samples* (N_{rej}), so that $N_{ice} = N_{acc} + N_{rej}$.

High confidence ROI test. Accurate extinction retrievals require a good estimate of the particle extinction-to-backscatter ratio (the "lidar ratio"). It is not uncommon for plate-like crystals to have a quasi-horizontal orientation. Specular lidar backscatter from these oriented crystals is much higher than from the more common randomly ori-

ented crystals, and these oriented crystals can be identified by their anomalously high backscatter and near-zero depolarization (Sassen, 1977; Noël and Sassen, 2005). Lidar ratios of layers containing HOI crystals are highly variable because the volume lidar backscatter is very sensitive to the relative concentrations of ROI and HOI. The result is that extinction retrievals of clouds containing HOI are highly uncertain (Mioche et al., 2010). Retrievals of layers without HOI but having low or medium phase confidence are also uncertain. Therefore, the AVD *Cloud_Phase* and *Phase_QA* flags are used to select only those samples identified as high-confidence ROI. The rejected HOI and low- or medium-confidence ROI sample counts are accumulated in N_{rej}.

Extinction quality control (QC) test. The outcome of each extinction retrieval is indicated in Level 2 products by the *Extinction_QC_532* flag. Only retrievals with *Extinction_QC_532* values of 0, 1, 2, 16, and 18 (see Table 3) are accepted for L3-ICE. Results from retrievals having other *Extinction_QC_532* values are rare but are excluded because they indicate either a failed retrieval or a retrieval which is likely to include erroneous values (Young et al., 2018). Table 3) lists the frequency with which these extinction QC values occur in Level 2 cloud data. In July 2008, roughly 80 % of extinction retrievals were performed on semi-transparent ice clouds, with the remaining retrievals performed on opaque clouds. A complete listing of all extinction QC flags assigned by the Version 4.20 algorithm is given in Table 2 of Young et al. (2018).

Extinction coefficient uncertainty. The uncertainty of each retrieved extinction value is estimated by the extinction retrieval algorithm and reported in L2-CPro. Divergence of the extinction uncertainty profile indicates a failed retrieval and range bins at and below the point of divergence are assigned an extinction uncertainty of 99.9 km^{-1}. These range bins are excluded, as are all bins at lower altitudes in the profile, since extinction solutions at lower altitudes depend critically on the extinctions retrieved in the above layer.

Accepted extinction range. Extinction values outside the range -0.1 to 10.0 km^{-1} are considered suspicious. In weakly scattering layers, signal noise can produce negative attenuated backscatter values, resulting in negative extinction coefficients and IWC values. Ignoring these negative values will result in a positive bias when computing means and medians. Therefore, a lower extinction limit of $-0.1\,\mathrm{km}^{-1}$ is used to retain negative extinction values resulting from signal noise while excluding large negative outliers resulting from erroneous retrievals. When cloud extinction is as large as 10.0 km^{-1} the signal is attenuated very rapidly and retrieval uncertainties become large. From Eq. (1), the maximum IWC corresponding to an extinction value of 10.0 km^{-1} is roughly 1.0 $\mathrm{g\,m}^{-3}$.

Ice clouds beneath water clouds. While it is common for precipitating ice to occur below supercooled water cloud layers (Zhang et al., 2010; Silber et al., 2021), fewer than 2 % of the ice layers detected by CALIOP are found beneath supercooled water layers. This is in part because most supercooled water layers are opaque to CALIOP. Retrievals of extinction profiles and optical depths of water clouds are only performed on layers averaged horizontally to 5 km or more. These retrievals are highly uncertain due to the difficulties of accounting for the effects of multiple scattering (Young et al., 2013) and also from averaging over a cloud that is horizontally inhomogeneous. Because these retrieval uncertainties propagate downward into the retrievals of underlying layers, retrievals of ice clouds beneath liquid clouds are highly uncertain. Therefore, the relatively few ice layer retrievals from beneath supercooled water layers are ignored.

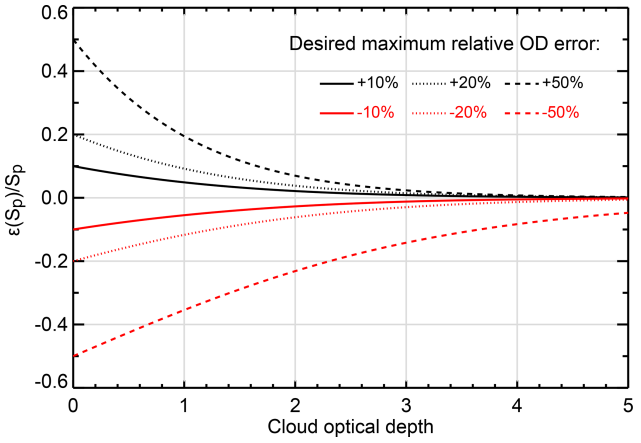

Figure 3. Lidar ratio accuracy required to achieve optical depth accuracy of 10 %, 20 %, or 50 %, based on Eq. (41) in Young et al. (2013).

Overlying optical depth threshold filter. As cloud optical depth increases, extinction retrievals become increasingly sensitive to errors in the lidar ratio used in the retrieval (Young et al., 2013). Under the condition of perfect calibration, constant scattering ratio within the cloud, and negligible multiple scattering, an exact expression for the relative error in retrieved cloud optical depth due to uncertainty in the particulate lidar ratio, S_{p}, is given by Eq. (41) in Young et al. (2013). Based on this equation, Fig. 3 shows the relative accuracy with which S_{p} must be estimated to retrieve cloud optical depth with a relative error of 10 %, 20 %, or 50 %. As seen in the figure, as optical depth approaches zero the relative optical depth error approaches the relative lidar ratio error: $\varepsilon(\tau_{\mathrm{p}})/\tau_{\mathrm{p}} = -\varepsilon(S_{\mathrm{p}})/S_{\mathrm{p}}$. Note that the required accuracy depends on the sign of the error and becomes increasingly asymmetric at greater optical depths.

Retrieving optical depths greater than 2 with even 50 % accuracy requires unreasonable accuracy in the lidar ratio used. Further, attenuation of the lidar backscatter signal significantly reduces the SNR. After penetrating an optical depth of 2, the attenuated backscatter signal is attenuated to less than 2 % of the unattenuated magnitude. Therefore, samples with overlying cloud optical depth greater than 2 are rejected

Table 3. Description of extinction quality control flags and their frequency of occurrence for ice cloud retrievals in July 2008 in Version 4.20 L2-CPro.

QC flag	Interpretation	Frequency
0	unconstrained retrieval; initial lidar ratio unchanged	0.616
1	constrained retrieval; solution constrained by measured two-way transmittance	0.191
2	unconstrained retrieval; initial lidar ratio reduced to achieve successful solutions for backscatter coefficients and uncertainties	0.007
16	feature identified as opaque, initial lidar ratio unchanged	0.074
18	feature identified as opaque; initial lidar ratio reduced to achieve successful solutions for backscatter coefficients and uncertainties	0.112
Others	unsuccessful retrievals of cloud extinction	< 0.001

and only ice cloud samples from the top two optical depths of the column are included in L3-ICE. Garnier et al. (2021) present statistics showing that, during daytime, nearly all ice clouds penetrated by the lidar signal have optical depths less than 2 and, at night, optical depths less than 3. Thus this filter mostly removes uncertain retrievals within opaque ice cloud layers.

Panels (e) and (f) of Fig. 2 show ice cloud extinction coefficient profiles before and after screening for high-quality extinction retrievals. Lines indicating overlying optical depth of 2 and the freezing level are the same as in panel (c). Comparison of panels (e) and (f) shows the most significant impact of applying quality filters is the exclusion of bins deep within opaque cloud layers where the overlying optical depth exceeds 2, as demonstrated near latitudes 19.0 and 11.0° N in this case study.

3.3 Product contents

CALIOP L3-ICE files are generated in Hierarchical Data Format 4 (HDF4) by the CALIPSO data management team and publicly distributed by NASA's Atmospheric Science Data Center (ASDC; https://asdc.larc.nasa.gov/project/CALIPSO/CAL_LID_L3_Ice_Cloud-Standard_V1-00, last access: 18 March 2024) and by the AERIS/ICARE data center (https://www.icare.univ-lille.fr/data-access/data-archive-access/?dir=CALIOP/CAL_LID_L3_Ice_Cloud.v1.00/, last access: 20 May 2024). Complete listings of all scientific datasets (SDSs) and metadata reported in these files are given in Appendix A and B. The primary contents of L3-ICE are histograms of ice cloud 532 nm extinction coefficients and IWC, and the associated gridded monthly sample counts (Table 2). Data are reported on a uniform three-dimensional global grid of 2.5° longitude by 2.0° latitude and 120 m vertical resolution. Extinction coefficients and IWC values of samples passing all the quality tests described above are aggregated into vertically resolved histograms and the sample counts listed in Table 2 are reported for each grid cell. The structure of the histograms is described in Table 4. Bins 2–43 contain extinction coefficient values between -0.1 and $10.0\,\mathrm{km}^{-1}$. The corresponding IWC values range from -0.01 to $1.0\,\mathrm{g\,m}^{-3}$. Retrieved values outside this range are flagged as outliers and, as a diagnostic, are reported in bins 1 and 44. Bins 17 and 18 contain samples near zero, with absolute magnitude less than $10^{-4}\,\mathrm{km}^{-1}$ and $10^{-5}\,\mathrm{g\,m}^{-3}$ for extinction and IWC, respectively.

To span the large range in extinction coefficient (σ) and IWC, the histograms are defined using logarithmic bin boundaries. In log space, the size of bins 2–43 is 0.2, thus five bins represent 1 order of magnitude. The definition of the bin boundaries is given below.

$$\text{Bin number of } \sigma = \begin{cases} 1 & -3.401\times10^{+38} < \sigma < -1.0\times10^{-1}, \\ \text{floor}\left(\frac{(-1.0)-\log_{10}|\sigma|}{0.2}+2\right) & -1.0\times10^{-1} \le \sigma < -1.0\times10^{-4}, \\ 17 & -1.0\times10^{-4} \le \sigma < 0, \\ 18 & 0 \le \sigma < +1.0\times10^{-4}, \\ \text{floor}\left(\frac{\log_{10}\sigma-(-4)}{0.2}+19\right) & +1.0\times10^{-4} \le \sigma < +1.0\times10^{+1}, \\ 44 & +1.0\times10^{+1} \le \sigma < +3.402\times10^{+38}. \end{cases} \tag{2}$$

$$\text{Bin number of IWC} = \begin{cases} 1 & -3.401\times10^{+38} < \text{IWC} < -1.0\times10^{-2}, \\ \text{floor}\left(\frac{(-2.0)-\log_{10}|\text{IWC}|}{0.2}+2\right) & -1.0\times10^{-2} \le \text{IWC} < -1.0\times10^{-5}, \\ 17 & -1.0\times10^{-5} \le \text{IWC} < 0, \\ 18 & 0 \le \text{IWC} < +1.0\times10^{-5}, \\ \text{floor}\left(\frac{\log_{10}\text{IWC}-(-5)}{0.2}+19\right) & +1.0\times10^{-5} \le \text{IWC} < +1.0\times10^{0}, \\ 44 & +1.0\times10^{0} \le \text{IWC} < +3.402\times10^{+38}. \end{cases} \tag{3}$$

Weighted summing over these histograms gives the monthly mean extinction (in km^{-1}) and IWC (in $\mathrm{g\,m}^{-3}$) in each 3D grid cell. The total number of valid ice cloud samples within a 3D grid cell is N_{acc}:

$$N_{\mathrm{acc}} = \sum_{i=1}^{44} N_{\mathrm{acc},i}\,, \tag{4}$$

where $N_{\mathrm{acc},i}$ is the number of accepted ice cloud samples in bin i of a histogram.

Table 4. Histogram bin ranges for ice cloud extinction coefficients and IWC. The bin number is calculated with Eqs. (2) and (3).

Bin number	σ bin boundaries, km^{-1}	IWC bin boundaries, $g\,m^{-3}$
1	$(-3.401 \times 10^{+38}, -1.0 \times 10^{-1})$	$(-3.401 \times 10^{+38}, -1.0 \times 10^{-2})$
2–16	$[-1.0 \times 10^{-1}, -1.0 \times 10^{-4})$	$[-1.0 \times 10^{-2}, -1.0 \times 10^{-5})$
17	$[-1.0 \times 10^{-4}, 0.0)$	$[-1.0 \times 10^{-5}, 0.0)$
18	$[0.0, +1.0 \times 10^{-4})$	$[0.0, +1.0 \times 10^{-5})$
19–43	$[+1.0 \times 10^{-4}, +1.0 \times 10^{+1})$	$[+1.0 \times 10^{-5}, +1.0 \times 10^{0})$
44	$[+1.0 \times 10^{+1}, +3.402 \times 10^{+38})$	$[+1.0 \times 10^{0}, +3.402 \times 10^{+38})$

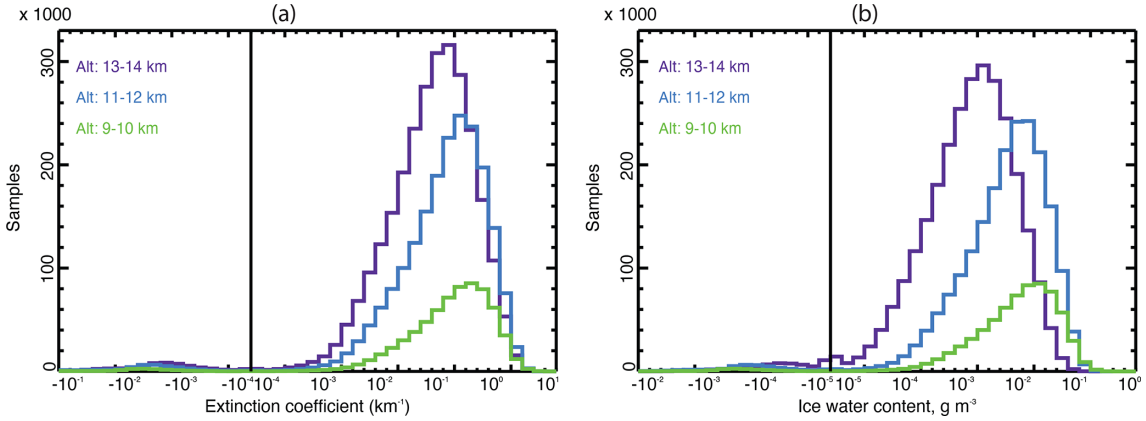

Figure 4. Histograms of night-time ice cloud 532 nm channel extinction coefficients **(a)** and IWC **(b)** observed at three altitudes in the tropics (23.5° S–23.5° N) in July 2008. The x axis is a split logarithmic scale to show both positive and negative values. The vertical solid line separates negative and positive values.

Figure 4 shows extinction coefficient and IWC histograms for three altitude ranges in the tropics in July 2008. The mode of the distributions moves to greater values as the altitude decreases and there are many more ice cloud samples detected in the highest altitude region between 13 and 14 km than in the lowest altitude region between 9 and 10 km. As histograms, even in log space, tend to be skewed, medians are provided as a second measure of the central tendency of the values. The differences in mean and median values (Table 5) are an indication of skewness and for some applications median values are more meaningful than averages. The median ice cloud extinction coefficient and IWC in each 3D grid cell are reported in the *Extinction_Coefficient_532_Median* and *Ice_Water_Content_Median* parameters.

The number of profiles acquired in each grid cell, over land and over ocean, are reported in the parameters *Land_Surface_Samples* and *Water_Surface_Samples*. The sum of these two parameters represents the total number of 5 km profiles acquired within each monthly grid cell. Ancillary data on atmospheric state and surface elevation are also included in the product. Surface elevation data are identical to that in L2-CPro (see Sect. 2). Gridded atmospheric state data include monthly mean temperature, pressure, and relative humidity, derived from the state data contained in L2-CPro. Full details of product contents can be found in the CALIPSO Data Products Catalog (Vaughan et al., 2022).

The spatial grid of L3-ICE was designed to be compatible with the grid of the Level 3 Tropospheric Aerosol product (Tackett et al., 2018) which is 5.0° longitude by 2.0° latitude and 60 m altitude. The altitude bins for both products are registered to the same lower altitude boundary. In Fig. 5, the vertical altitude grid used in L3-ICE is compared to the vertical grids used in L2-CPro and in the Level 3 Tropospheric Aerosol product. In L2-CPro, the AVD is reported at 60 m vertical resolution between 8.2 and 20.2 km but reported at 30 m vertical resolution below 8.2 km, while the vertical resolution of L3-ICE is 60 m at all altitudes. Using the AVD feature type information, a 60 m range bin below 8.2 km in L3-ICE is defined as cloudy when the feature type of at least one of the two 30 m AVD values is "cloud". If either the upper or lower 30 m bin is classified as ice, then the entire 60 m grid cell is considered to be ice cloud, regardless of the classification of the non-ice bin. When aggregating two 60 m bins to one L3-ICE 120 m vertical bin, each 60 m cloudy bin is considered as one sample count; thus, the sample count in this L3-ICE 120 m bin would be two. This aggregation method from fine vertical bin to coarse vertical bin is analogous to accumulating Level 2 passive sensor data with a spatial scale

Table 5. Mean and median values of histograms in Fig. 4.

	Extinction coefficient, km^{-1}			IWC, $g\,m^{-3}$		
Altitude	13–14 km	11–12 km	9–10 km	13–14 km	11–12 km	9–10 km
Mean	0.2891	0.4391	0.5386	0.006145	0.02041	0.03108
Median	0.1292	0.2048	0.3246	0.002048	0.008155	0.01292

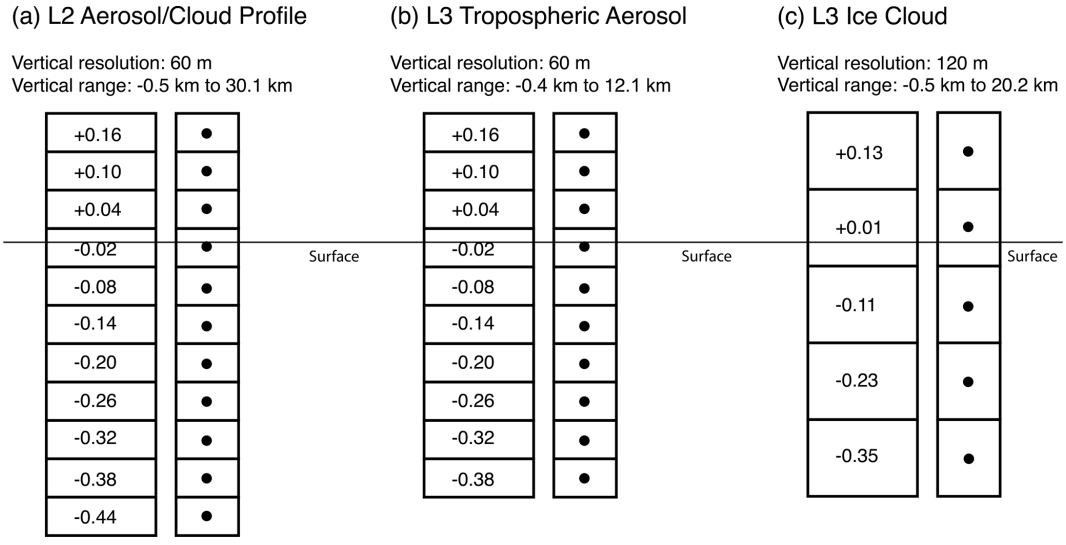

Figure 5. Panel **(a)** shows the vertical grid resolution and vertical range of Level 2 Aerosol/Cloud Profile products for the lowest altitudes in the profiles. Panels **(b)** and **(c)** show the same information for the Level 3 Tropospheric Aerosol product and L3-ICE, respectively. The numbers on the left column of panel **(a)** are the lidar altitudes with respect to mean sea level, represented by the horizontal line, which are registered to the center of the vertical bins as shown as dots on the right. Note the centers of L3-ICE altitude bins are at the center of every two neighboring vertical bins in the Level 2 Aerosol/Cloud Profile products and the Level 3 Tropospheric Aerosol product.

of tens of kilometers, for example, into a Level 3 coarse horizontal grid such as 1.0° longitude by 1.0° latitude.

4 Data use examples

L3-ICE reports vertically resolved parameters derived from active sensor measurements. Therefore, the design and contents of the product are somewhat, or even substantially, different from commonly used passive sensor data products. This section presents several data usage examples, to illustrate a few characteristics of the product.

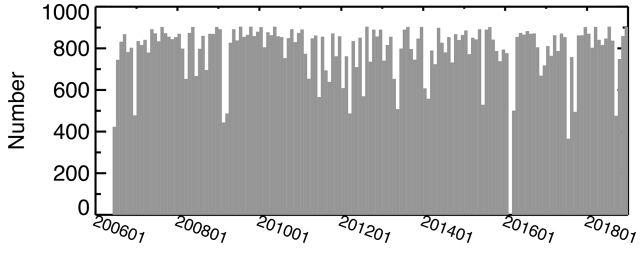

Figure 6. The total numbers of processed Level 2 5 km Cloud Profile product files, including both daytime and nighttime granules, used in the V1.00 L3-ICE product.

4.1 Temporal coverage

CALIOP Level 2 data is organized into granules, with each orbit containing one daytime granule and one nighttime granule. Temporal coverage over the life of the CALIPSO mission is fairly uniform. Figure 6 shows the number of granules used to compute each of the monthly average Level 3 files from the beginning of data acquisition in June 2006 to the end of 2018. Monthly data coverage varies somewhat month-to-month due to various payload operations that impact data acquisition. For each L3-ICE file, the number of L2-CPro product files used is reported as *Number_of_Level2_Files_Analyzed* in the L3-ICE file metadata. A list of the L2-CPro file names is provided in the *List_of_Input_Files* metadata filed. The largest gaps in sampling are 3 weeks in February and March 2009, due to the switchover between the primary and backup lasers, and about 45 d from the end of January until mid-March 2016 caused by a GPS clock problem that affected the entire spacecraft. Detailed information on CALIOP data outages is available

on the CALIPSO website at https://www-calipso.larc.nasa.gov/tools/instrument_status/ (last access: 21 May 2024).

4.2 Computing height-resolved zonal means

Mean profiles of in-cloud and all-sky IWC can be computed from the L3-ICE parameters *Ice_Water_Content_Histogram* ($N_{\mathrm{acc},i}$) and *Ice_Water_Content_Bin_Boundary* (IWC_i) as shown in Eqs. (5) and (6). In these calculations, the outliers in bins 1 and 44 are excluded from the numerators and the denominator of both equations. In-cloud IWC is computed as

$$\mathrm{IWC}_{\mathrm{in-cloud}} = \frac{\sum_{i=2}^{43} N_{\mathrm{acc},i} \times \mathrm{IWC}_i}{\sum_{i=2}^{43} N_{\mathrm{acc},i}}, \tag{5}$$

where $N_{\mathrm{acc},i}$ and IWC_i are the accepted ice cloud sample count and the mean of the upper and lower bin boundaries for the IWC boundaries of histogram bin i and N_{acc}. All-sky IWC can be computed as

$$\mathrm{IWC}_{\mathrm{all-sky}} = \frac{\sum_{i=2}^{43} N_{\mathrm{acc},i} \times \mathrm{IWC}_i}{N_{\mathrm{cld}} + N_{\mathrm{clr}}}. \tag{6}$$

Figure 7 shows the zonal annual mean occurrence frequency of accepted ice cloud (HC ROI) defined as $N_{\mathrm{acc}}/(N_{\mathrm{cld}} + N_{\mathrm{clr}})$ and the corresponding zonal-mean in-cloud IWC and all-sky IWC for day and for night, calculated using Eqs. (5) and (6). Zonal patterns of monthly averages are asymmetric about the Equator but annually averaged distributions are quite symmetric. The tropical tropopause layer can be seen as a region of low IWC from 30° S to 30° N and above roughly 14 km. Polar stratospheric clouds (PSCs) occurring in Antarctic winter can be seen above 12 km at high southern latitudes. PSCs occurring below the 20.2 km upper limit of L3-ICE are included in the product whenever they meet all quality screening requirements.

Figure 7d and f show a general pattern of increasing in-cloud IWC as altitude decreases while the all-sky IWC (Fig. 7h and j) shows a rainbow-shaped maximum which varies between 6 and 12 km with latitude. The decrease in all-sky average IWC below this maximum is due to the increasing frequency of complete attenuation of the lidar signal in optically dense clouds. Small differences in zonal-mean distributions can be seen between day (left) and night (right). The solar background decreases the daytime CALIOP SNR, degrading detection sensitivity that preferentially affects weakly scattering layers. This leads to cloud occurrence which is somewhat higher at night than during day, and there are corresponding small increases in nighttime IWC relative to daytime.

The same method applies to ice cloud extinction coefficient. To derive the in-cloud and all-sky extinction coefficients, the *Ice_Water_Content_Histogram* and *Ice_Water_Content_Bin_Boundary* parameters in Eqs. (5) and (6) are replaced with *Extinction_Coefficient_532_Histogram* and *Extinction_Coefficient_532_Bin_Boundary*.

Figure 8 shows how quality screening applied to the L2-CPro data affects ice cloud occurrence frequencies reported in L3-ICE. Figure 8a shows zonal-mean cloud occurrence for July 2008, before quality screening, computed as $N_{\mathrm{ice}}/(N_{\mathrm{cld}} + N_{\mathrm{clr}})$. Figure 8b shows the same data after quality screening, computed as $N_{\mathrm{acc}}/(N_{\mathrm{cld}} + N_{\mathrm{clr}})$. Figure 8c shows the difference in the unscreened and screened data. Relatively few samples are removed at high altitudes. A large fraction of ice clouds is removed in the lower troposphere due to the increasing uncertainty in the retrievals as overlying optical depth increases. The screening completely removes samples at low altitudes in the tropics which were initially classified as low- or medium-confidence ice clouds at altitudes too warm for ice to occur. A few low-confidence samples above the tropical tropopause are also removed.

It is noticed that a discontinuity appears around 4 km in mean zonal IWC and extinction coefficient patterns in Fig. 7 and the percentage of removed ice cloud samples in Fig. 8. This discontinuity is likely due to boundary layer cloud-clearing process in the Level 2 feature detection algorithm (Vaughan et al., 2005, 2009). This chosen boundary of 4 km might result a small artificial discontinuity at this altitude if accumulating data over a long duration such as 1 month. More details related to the boundary layer cloud-clearing process are provided in Sect. 5.3. A user should be cautious when interpreting IWC and ice cloud extinction coefficient below or around 4 km since ice clouds are rarely formed below 4 km and the artificial discontinuity possibly due to the boundary layer cloud-clearing process.

4.3 Computing meridional means

Figure 9 shows meridional annual average in-cloud and all-sky IWC in 2008 during both day and night between 30° S and 30° N. Means are computed using Eqs. (5) and (6), as for zonal means. As in the zonal plots, there is a general tendency for in-cloud IWC to increase with decreasing altitude down to the freezing level at about 3 km and for all-sky IWC to have a maximum in the upper troposphere. Frequent occurrence of clouds above 12 km altitude is associated with well-known regions of frequent deep convection in the western Pacific, the Amazon basin, and central Africa.

4.4 Anomaly of ice cloud occurrence frequency and IWC

Figure 10 shows the deseasonalized time series of monthly zonal ice cloud occurrence and all-sky IWC anomaly from 2006 to 2018. The global zonal means (82° N–82° S) are computed from monthly zonal profile data. A sudden increase in both cloud occurrence and IWC is seen in Decem-

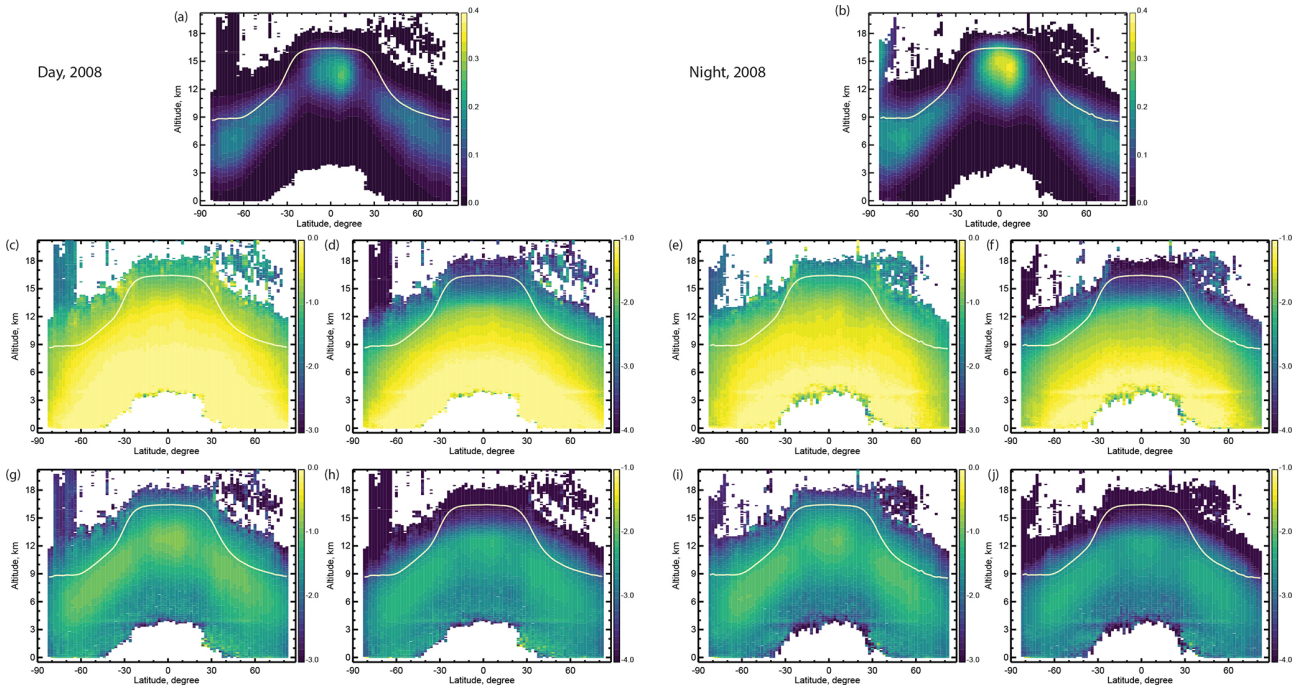

Figure 7. Annual zonal-mean ice cloud occurrence frequency **(a, b)**, in-cloud extinction coefficient in km^{-1} **(c, e)**, in-cloud IWC in $g\,m^{-3}$ **(d, f)**, all-sky extinction coefficient in km^{-1} **(g, i)**, and all-sky IWC in $g\,m^{-3}$ **(h, j)** for 2008 at the L3-ICE resolution of 2.0° latitude and 120 m altitude. Color bars for extinction coefficient and IWC are logarithmic. The white line indicates zonal annual mean tropopause height. Left: day; right: night.

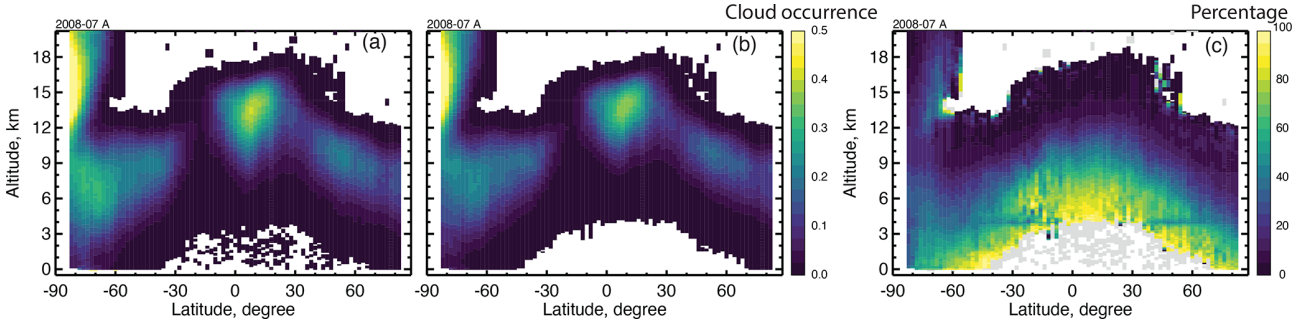

Figure 8. Zonal ice cloud occurrence frequency for July 2008 (night) before **(a)** and after **(b)** filtering. Cloud occurrence from 0 to 0.5 is coded in color. Panel **(c)** plots the percentage of samples removed by filtering ($(100 \times N_{rej}/N_{ice})\,\%$) with gray representing 100 % removal.

ber 2007 below an altitude of 12 km. This corresponds to a permanent change in the view angle of CALIOP from 0.3 to 3.0° on 28 November 2007 and is related to the detection of HOI particles, which are often found together with ROI within a cloud layer. HOI are readily detected at a view angle of 0.3°, but at 3.0° the backscatter returns from HOI are greatly reduced and clouds are more often classified as ROI. Because cloud layers identified as HOI are removed during quality screening, the occurrence of ROI increases suddenly in December 2007 when fewer clouds containing HOI are identified and removed. Anomalies at the highest altitudes are above the altitude of the tropical tropopause and are driven by the occurrence of polar stratospheric clouds, which tend to occur during polar winter and exhibit large year–year variability (Pitts et al., 2018).

5 Uncertainties and biases

As a cloud sensor, CALIOP has the advantages of high detection sensitivity and accurate height determination, but the data products are subject to several sources of uncertainty which deserve discussion. In particular, here we focus on incomplete penetration of dense clouds, the nadir-only zero-swath observing geometry, and artifacts due to the way single-shot cloud clearing is performed in Version 4.2 Level 2 processing.

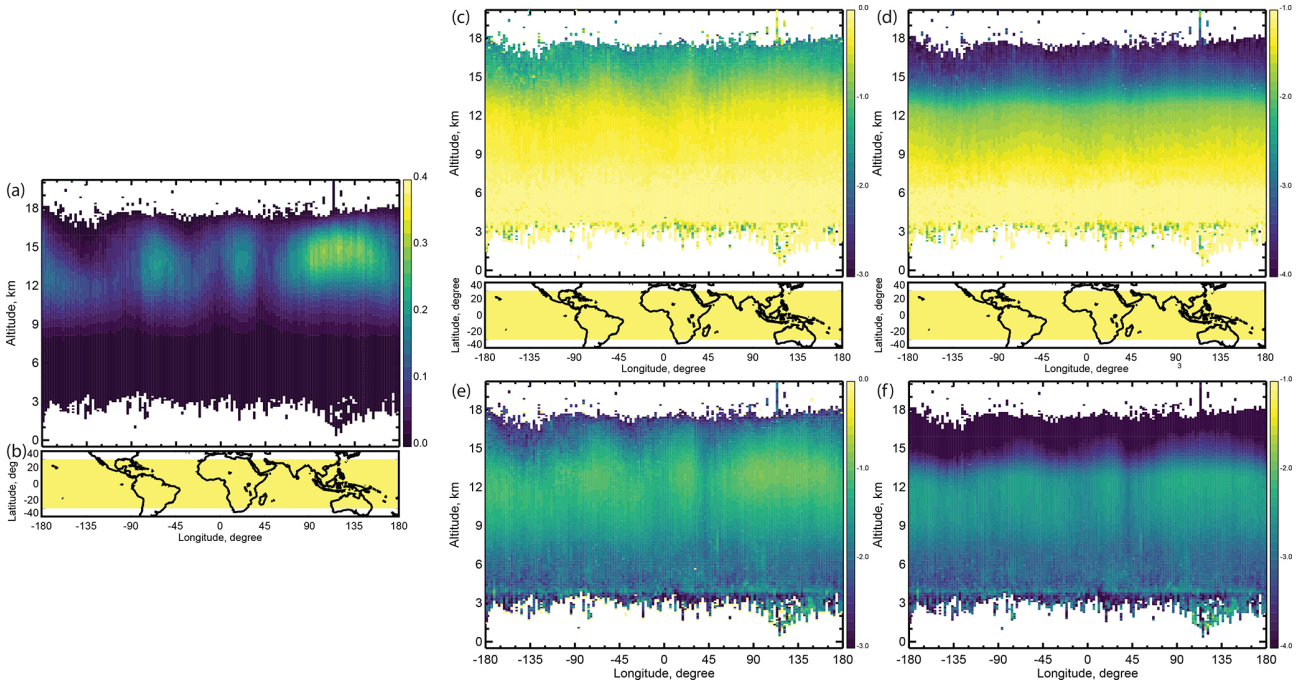

Figure 9. Annual-mean meridional distributions between 30° S and 30° N in 2008 (day + night). **(a)** Accepted ice cloud occurrence frequency; **(b)** map with yellow shaded area representing tropics between 30° S and 30° N; **(c)** mean in-cloud extinction coefficient in km^{-1}; **(d)** mean in-cloud IWC in $\mathrm{g\,m}^{-3}$; **(e)** mean all-sky extinction coefficient in km^{-1}; **(f)** mean all-sky IWC in $\mathrm{g\,m}^{-3}$.

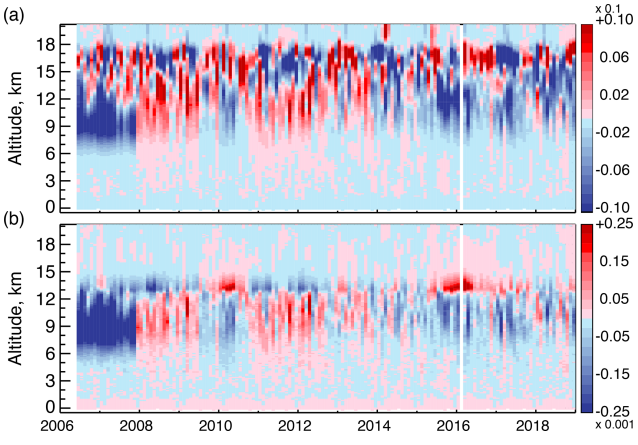

Figure 10. Deseasonalized time series of monthly global anomalies of **(a)** ice cloud occurrence frequency and **(b)** all-sky IWC from 2006 to 2018. Color coding indicates relative variation from the mean with a range of ±2 % for ice cloud occurrence frequency and $\pm 0.25 \times 10^{-3}\,\mathrm{g\,m}^{-3}$ for IWC. The blue regions below 12 km and prior to December 2007 show the impact of the different sensitivities of CALIOP to HOI at view angles of 0.3° (prior to December 2007) and at 3.0°.

5.1 Penetration of dense clouds

The CALIOP backscatter signal becomes totally attenuated within optically thick clouds so that only the upper parts of dense clouds are observed. Figure 11a shows the all-sky fraction of Level 2 profiles that reach a given altitude, or the surface, before being completely attenuated, $f_{\mathrm{obs}}(z)$:

$$f_{\mathrm{obs}}(z) = \frac{1}{N_{\mathrm{tot}}} \sum (N_{\mathrm{cld}} + N_{\mathrm{clr}}) = 1 - \frac{1}{N_{\mathrm{tot}}} \sum N_{\mathrm{atten}}, \qquad (7)$$

where $N_{\mathrm{tot}} = N_{\mathrm{cld}} + N_{\mathrm{clr}} + N_{\mathrm{atten}}$. It can be seen in Fig. 11a that penetration to the freezing level is quite frequent in the tropics and subtropics, except in the core of the Inter-Tropical Convergence Zone (ITCZ). Significant blockage begins to occur at roughly the −25 °C level where supercooled water clouds, which tend to be opaque to the lidar signal, begin to occur frequently.

As discussed earlier, data included in L3-ICE are restricted to samples where the overlying optical depth is less than 2, which sets a limit on the maximum ice water path (IWP) reported in the product. A rough estimate of this limit can be easily derived if all the ice in the column is assumed to be at an altitude corresponding to temperature T_0. In that case, the maximum value of IWP set by an optical depth limit of τ_{max} is given by

$$\mathrm{IWP}_{\mathrm{max}}(T_0) = \frac{\mathrm{IWC}}{\sigma}(T_0) \int \sigma(z)\mathrm{d}z = \tau_{\mathrm{max}} \frac{\mathrm{IWC}}{\sigma}(T_0). \qquad (8)$$

Figure 12 plots the temperature-dependent value of IWC/σ, given by Eq. (1), and the corresponding maximum IWP based on Eq. (8). For $\tau_{\mathrm{max}} = 2$, the maximum retrievable IWP corresponding to an overlying optical depth of 2

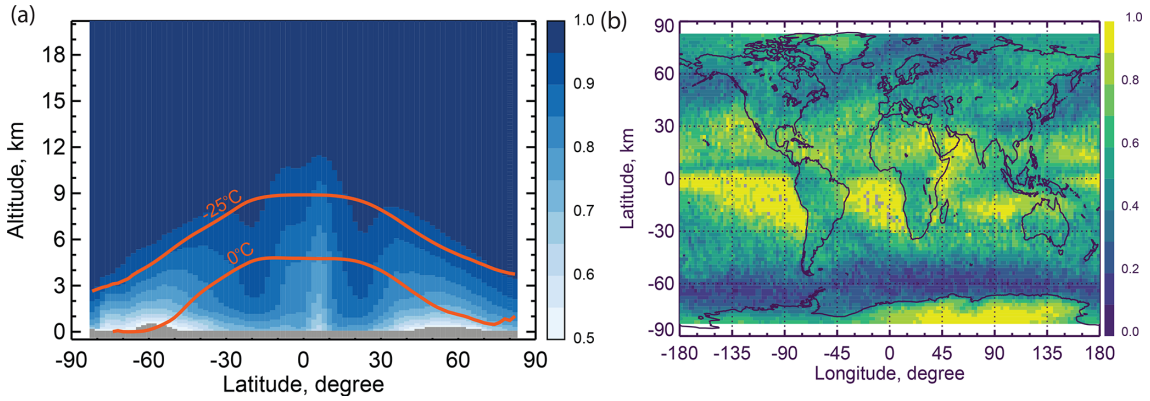

Figure 11. **(a)** Fraction of Level 2 5 km profiles reaching a given altitude before becoming fully attenuated, annual average for 2008. Mean surface and subsurface below, determined from lidar detection, or from the DEM if the signal has been fully attenuated, are shaded in gray; **(b)** fraction of cloudy profiles where cloud optical depth above the freezing level is less than 2, for 2008.

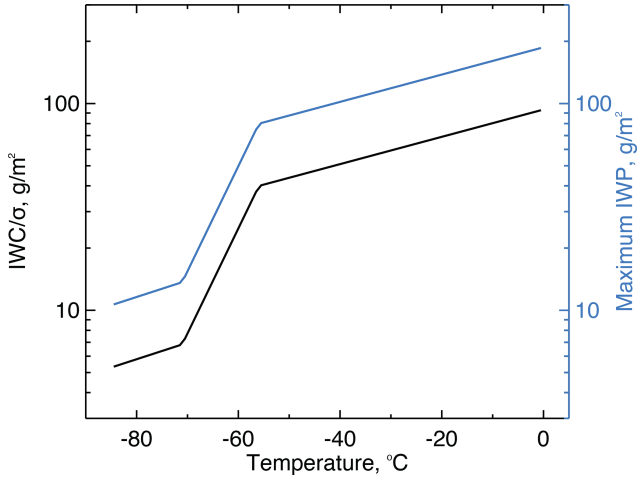

Figure 12. Temperature-dependence of the IWC-to-σ ratio used to estimate IWC from retrieved extinction (Eq. 1, black line) and the limit on IWP due to the requirement that the overlying cloud optical depth is less than 2 (blue line).

is about 200 g m^{-2}. The maximum reported IWP decreases with temperature to less than 20 g m^{-2} for very cold clouds found in the tropical tropopause layer, driven primarily by decreasing effective particle size.

For a sense of the extent to which dense clouds impact the ability of CALIOP to detect and retrieve all the ice clouds in the atmospheric column, Fig. 11b shows the geographical distribution of the frequency with which the freezing level is reached before penetrating a cloud optical depth of 2. The spatial structure in Fig. 11b reflects well-known features of the global cloud distribution, driven by the general circulation of the atmosphere, such as the ITCZ. In subtropical subsidence regions and over deserts, where there are few convective or mid-level clouds, CALIOP often observes the entire column above the freezing level. In mid- and high-latitude regions, penetration to the freezing level is blocked by frontal storms and, in fair weather, can be blocked by supercooled water clouds. This topic will be explored further in Sect. 6.

5.2 Sampling considerations

CALIOP is a nadir-viewing sensor whose measurements are in the form of zero-swath vertical curtains. Relative to passive imagers, horizontal spatial sampling from CALIOP is very sparse and cloud properties within a grid cell are estimated from just a few orbit tracks leading to a "representativity uncertainty". Prior to September 2018, when the satellite altitude was lowered to resume formation flying with CloudSat, the orbit track of CALIPSO was controlled to repeat a fixed pattern of 233 orbits every 16 d. At the Equator, the 233 orbit tracks are spaced by about 1.5° longitude, and some cells of the often-used 1.0° × 1.0° global grid are never sampled. The 2.0° × 2.5° lat–long grid chosen for L3-ICE is a compromise between high longitudinal resolution and the desire to sample every grid cell. The grid exactly overlaps that of the 2.0° × 5.0° lat–long grid of the Level 3 Aerosol Profile product (Winker et al., 2013) but with twice the longitudinal resolution.

Figure 13 shows the monthly sampling provided by CALIOP. Only seven or eight orbit tracks pass through a typical grid cell in 1 month, except at high latitudes. Sampling theory can be used to examine uncertainties in sampling areal quantities such as mean cloud cover from transect measurements (Key, 1993). Results presented in Winker et al. (2017) show that uncertainties due to the sparse sampling of CALIOP can be reduced significantly by averaging spatially and/or temporally. Kotarba and Solecki (2021) took a more comprehensive approach using bootstrapped confidence intervals to examine representativity uncertainty in CALIOP estimates of cloud amount. They found that confidence intervals decreased (i.e., improved) in rough proportion to the number of samples when observations were aver-

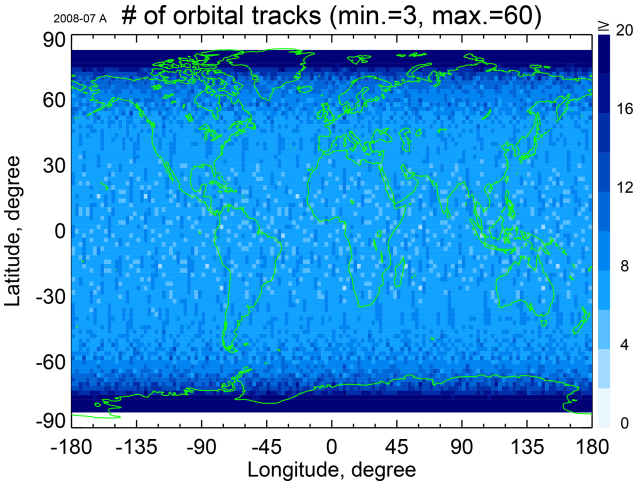

Figure 13. Number of tracks per month through a 2.0° × 2.5° lat–long grid cell in July 2008 (day + night).

aged over coarser grids or longer time periods. A subsequent study examining the impacts of representativity uncertainty on the accuracy of mean annual cloud amount, cloud optical depth, and cloud top height found that representativity errors for cloud amount and cloud optical depth behaved similarly with averaging (Kotarba, 2022). For these reasons, data are reported in L3-ICE as sample counts to facilitate proper aggregation to larger, and statistically more meaningful, space-time scales.

To give an observation-based view of the representativity uncertainty due to sparse spatial sampling, 60 consecutive days of L2-CPro data were numbered from 1 to 60. IWP was computed by vertically integrating IWC for each grid cell from even-numbered days and from odd-numbered days. Figure 14 shows distributions of absolute difference $|\mathrm{IWP_{odd}} - \mathrm{IWP_{even}}|$ and relative difference $|\mathrm{IWP_{odd}} - \mathrm{IWP_{even}}|/[0.5(\mathrm{IWP_{odd}} + \mathrm{IWP_{even}})]$ between IWP from odd and even days at the spatial resolution of L3-ICE (black) and when averaged using a 10° × 10° (red) and 10° × 20° (blue) degree lat–long grid. The hypothesis is that if a grid cell is well-sampled, the 30 d averaged IWP should be similar whether using even or odd days. The figures show how large differences using the L3-ICE 2.0° × 2.5° degree lat–long grid can be significantly reduced by averaging to coarser resolutions. Figure 15 shows the greater averaging of zonal means involve enough averaging that odd-day and even-day IWP agree quite well, using either 2.0 or 10° latitude increments.

5.3 Impact of clearing single-shot ice clouds

The CALIOP Level 2 feature detection algorithm includes a boundary layer cloud-clearing process to mitigate potential cloud contamination when retrieving aerosol optical properties (Vaughan et al., 2005, 2009). Data within layers initially detected at CALIOP's fundamental 5 km (15 laser shots) along-track resolution are re-examined at single-shot resolution. If clouds with top altitudes at or below 4.0 km are intermittently detected in single-shot profiles, the attenuated backscatter data within these clouds are removed and the remaining single-shot data are re-averaged to a coarser spatial resolution (i.e., 5, 20, or 80 km). The homogenized layers detected within these coarser cloud-cleared averages can then be confidently classified by the CALIOP cloud–aerosol discrimination (CAD) algorithm (Liu et al., 2019). If clouds with tops $\leq$ 4.0 km are detected at single-shot resolution in all 15 profiles within a 5 km average, the data removal and re-averaging process is not executed. Instead, the layer initially detected at 5 km resolution is classified a priori as a cloud, by virtue of having clouds detected within all single-shot profiles comprising the 5 km average. Note that clouds detected at single-shot resolution with tops above 4.0 km are not subject to the cloud-clearing process.

As intended, this clearing process removes strongly scattering water and ice clouds and avoids most of the potential cloud contamination of aerosol in averaged profiles. However, one unforeseen side effect is that the strong scattering from ice clouds detected at single-shot resolution can be removed from the (cloud-cleared) layers subsequently identified as ice clouds in the L2-CPro data. Consequently, biases may exist in the L2-CPro cloud phase assessments, along with the corresponding extinction coefficient and IWC profiles, for low altitude ice clouds detected in polar regions.

The clearing of single-shot features only impacts L2-CPro ice cloud extinction and IWC at high latitudes, as ice clouds are rarely found below 4.0 km altitude at low latitudes. Figure 16a shows the occurrence of ice clouds with cloud tops below 4.0 km is limited primarily to latitudes poleward of 60°. Figure 16b shows the fraction of high-confidence ROI clouds from which single-shot profiles have been cleared. It can be seen that less than 10 % of low altitude 5 km ice clouds are affected by the removal of single-shot layers.

6 Comparison with DARDAR and 2C-ICE products

There are currently two radar–lidar products which derive ice cloud extinction and IWC profiles from joint CALIOP and CloudSat observations using an optical estimation technique: 2C-ICE (Deng et al., 2010, 2015) and DARDAR (Delanoë and Hogan, 2010; Cazenave et al., 2019). The combined capabilities of lidar and 94 GHz cloud profiling radar provide sensitivity to nearly the full spectrum of atmospheric ice, from subvisible cirrus particles to precipitating ice. Additionally, a joint radar–lidar retrieval can, in principle, retrieve vertical profiles of effective particle size and lidar extinction consistent with the observed radar reflectivity and lidar attenuated backscatter. As IWC is a function of effective particle size, this is an attractive approach to IWC retrievals. In strong convection, however, attenuation of CloudSat W-band can be

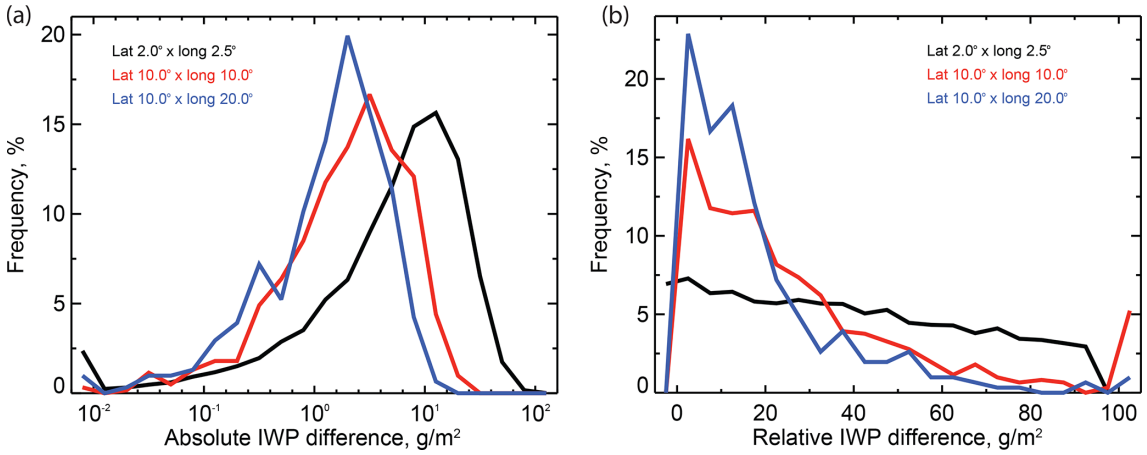

Figure 14. Absolute and relative differences between IWP computed from odd and even days using 2.0° × 2.5°, 10° × 10°, and 10° × 20° lat–long grid cells.

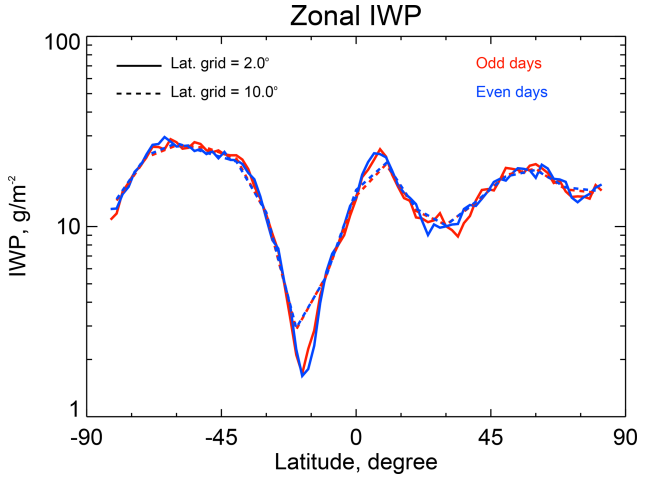

Figure 15. Zonal-mean IWP computed from 30 odd days (red) and from 30 even days (blue) for latitudinal resolution of 2.0° (solid lines) and 10° (dashed lines).

significant, leading to errors in the DARDAR and 2C-ICE products.

In this section we compare L3-ICE with the 2C-ICE and DARDAR products. We first compare how a selected scene is represented in the three products. Then, to characterize differences at space-time scales of typical interest, we aggregate all available data from 2C-ICE and DARDAR over 1 month using the same methodology used to construct L3-ICE. These comparisons illustrate similarities and differences a data user might find when using the products at monthly scales. In conducting these studies, we will restrict our comparisons to those that directly illustrate some salient aspect of the L3-ICE data. Interpretation of differences between DARDAR and 2C-ICE fall outside our scope and have not been pursued.

Figure 17 compares how the scene shown in Fig. 2 is reported in the CALIOP products and in the DARDAR and 2C-ICE products. The top row compares the three cloud masks. Figure 17h and i are the same as Fig. 2c and f, showing the L2-CPro cloud mask and extinction profiles using the filtering of L3-ICE. The high-confidence ice layers (HC ROI) selected for L3-ICE are shown in white (Fig. 17g) and the locations of liquid water clouds, mostly supercooled, are shown in blue. Black dots indicate the altitude where the overlying optical depth equals 2.

Ice clouds composed of small particles are not detected by the radar, while the lower parts of optically thick clouds are not seen by the lidar. A previous study found that the region of radar–lidar overlap is roughly −50 to −20 °C and that less than half of clouds colder than −50 °C (above about 12 km in the tropics) are detected by CloudSat (H14, Fig. 1). The DARDAR and 2C-ICE algorithms are designed to retrieve all three regions – lidar-only, radar–lidar overlap, and radar-only – in a consistent manner. In the lidar-only region, a radar reflectivity profile is estimated from the Level 1 lidar profile, based on a microphysical model, and a lidar attenuated backscatter profile is estimated in a similar way in the radar-only region. In this way, a single retrieval algorithm can be applied in a consistent way throughout the entire depth of the cloud, whether the cloud is detected by both radar and lidar or only by one of the instruments. The DARDAR (Fig. 17a) and 2C-ICE (Fig. 17d) masks are color coded to show the three regions. While the 2C-ICE cloud mask reports only ice clouds, between 0 and −40 °C the DARDAR cloud mask can report ice, supercooled liquid, or mixed phase if both ice and liquid occur within the same measurement volume. The green areas in Fig. 17a indicate either supercooled liquid or mixed-phase clouds. As expected, the regions corresponding to radar-only regions are not seen in the L3-ICE mask. Ice shown at lower altitudes, down to about 4.0 km, in the DARDAR and 2C-ICE masks is not detected by CALIOP because

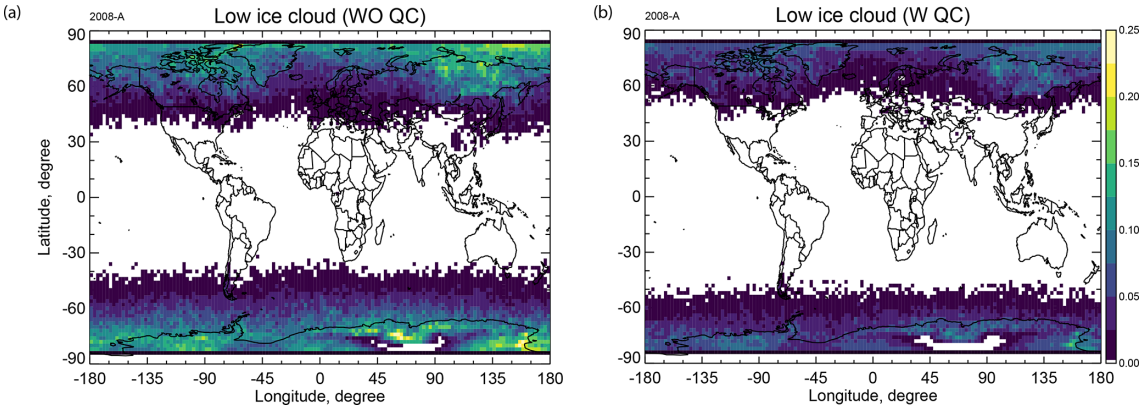

Figure 16. **(a)** Annual mean frequency of occurrence of ice clouds below 4.0 km altitude for 2008; **(b)** fraction of high-confidence ROI clouds below 4.0 km with one more single-shot ice clouds removed.

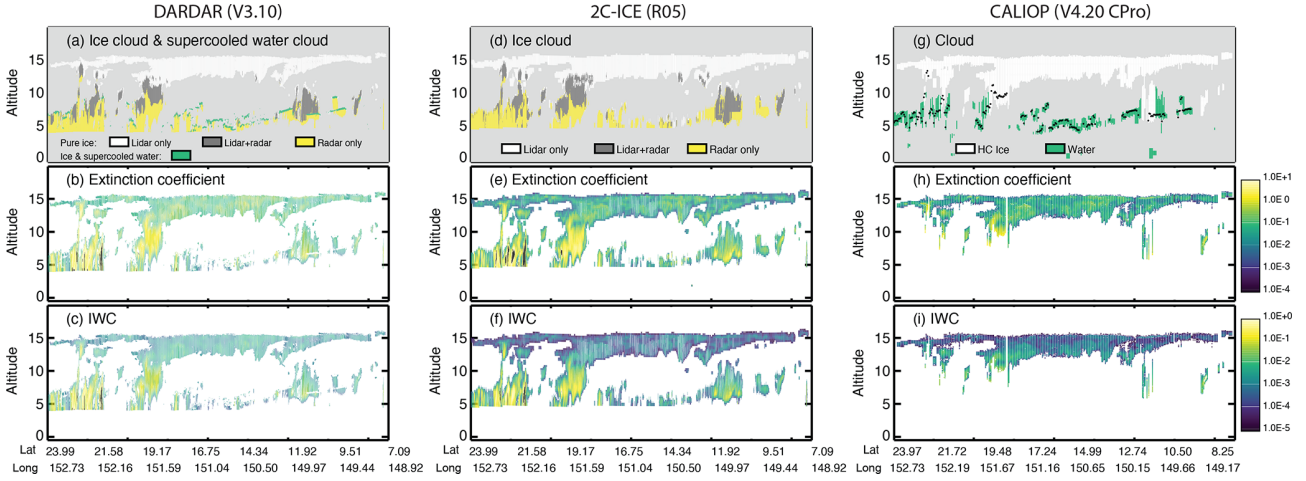

Figure 17. Comparison of the DARDAR and 2C-ICE products with L2-CPro, using the filtering of L3-ICE, for the same scene as Fig. 2. Panels **(a)**, **(d)**, and **(g)** show results from the three feature masks. Lidar-only, overlap, and radar-only regions are color coded in **(a)** and **(b)**. Black dots in **(g)** indicate the level where the overlying optical depth is 2. Ice cloud extinction coefficients (km^{-1}) are compared in **(b)**, **(e)**, and **(h)**, and IWC ($g\,m^{-3}$) is compared in **(c)**, **(f)**, and **(i)**.

of blockage by the supercooled water clouds and, in a few places, by dense overlying ice clouds.

The second and third rows of Fig. 17 compare ice cloud extinction and IWC, respectively. The cirrus layer above 10 km is optically thin and fully retrieved in L2-CPro but the overlying optical depth 2 limit is often exceeded within the supercooled water layers, blocking CALIOP's view of lower layers. Denser convective clouds are seen near 20 and 22° N. The two joint products retrieve the denser ice in these convective regions, which are not detected by CALIOP due to attenuation within the overlying clouds. Extinction and IWC retrievals in the upper cloud layer, which is mostly sensed only by lidar, are similar in L3-ICE and 2C-ICE, but the extinction and IWC retrieved by DARDAR in this region are noticeably higher than the other two products.

To provide a perspective on the ability of lidar to probe dense ice clouds, Fig. 18 compares frequency distributions of IWP values derived from the three products. Dashed lines show IWP values from L3-ICE and computed from monthly averages of DARDAR and 2C-ICE IWC profile data using the L3-ICE lat–long grid. Solid lines show the frequency distributions of IWP values computed directly from the Level 2 IWC profile data. Data selection for all cases is the same as that used to produce L3-ICE, as described in Sect. 3.1. The frequency distributions of DARDAR and 2C-ICE are quite similar except for very large and very small IWP. As discussed in Sect. 5.1, the maximum IWP which can be reliably retrieved from CALIOP is about 200 $g\,m^{-2}$. This causes the IWP frequency distribution of L3-ICE to be distorted relative to that of the radar–lidar products, as CALIOP fails to fully penetrate columns with very high IWP. The frequency distributions in Fig. 18 are in better agreement for IWP values less than 1 $g\,m^{-2}$, where DARDAR and 2C-ICE rely heavily on the lidar observations. Differences between IWP computed

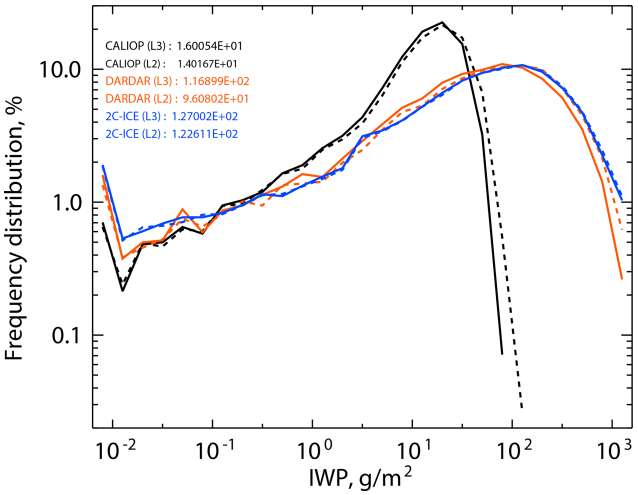

Figure 18. Frequency distributions of IWP computed from L3-ICE, DARDAR, and 2C-ICE for all latitudes in July 2008. Solid lines show IWP computed from Level 2 products (along-track curtains). Dashed lines represent IWP computed from monthly grid-cell averages. Legend shows global mean IWP (g m^{-2}).

from Level 2 IWC data and from gridded monthly averaged Level 3 IWC data are expected because the vertical correlations of cloud overlap are lost in the monthly averaged data, but these differences are seen to be small for all three products.

To give further perspective on differences in the information content of L3-ICE and the two radar–lidar products, Fig. 19a–c compare ice cloud occurrence frequency, zonal-mean all-sky profiles of ice cloud extinction, and IWC occurrence in the northern tropics from the three products. In these figures we averaged all the available data in each product, except that profile data were screened to remove points that represent fewer than 200 samples. Results for other latitude bands are shown in the Supplement. The DARDAR and 2C-ICE IWC profiles tend to agree much better with each other than with L3-ICE, but it is notable that there are significant differences between all three products in ice cloud occurrence frequencies at most altitudes. Below 13 km, all-sky extinction coefficients and IWC from DARDAR and 2C-ICE agree reasonably well with each other but values from L3-ICE are significantly less. These smaller all-sky values of L3-ICE extinction coefficient and IWC are driven by blockage of the lidar signal in optically thick clouds as can be seen in Fig. 19a, where the lidar is able to detect many fewer clouds than the radar at lower altitudes. Above 12 km, however, cloud occurrence from L3-ICE is higher than from DARDAR but similar or somewhat lower than from 2C-ICE. The all-sky IWC profiles show similar features except that DARDAR and 2C-ICE both have greater IWC at high altitudes than L3-ICE and agree relatively well at all altitudes, in spite of DARDAR and 2C-ICE cloud occurrence being noticeably different at intermediate altitudes (Fig. 19a).

Figure 19d and e compare in-cloud profiles of extinction and IWC from the three products. This removes the differences between the all-sky extinction coefficient and IWC profiles, which are due to differences in cloud occurrence. While significant differences are still present, values from L3-ICE below 10 km are only a factor of 3 to 5 lower than the other two products. This remaining difference may be due, at least in part, to the ice clouds at these altitudes, which are blocked from being viewed by CALIOP but are retrieved by radar, being denser than the ice clouds that are seen by CALIOP.

The cloud mask algorithms associated with L3-ICE, DARDAR, and 2C-ICE are quite different, and each algorithm is optimized according to the objectives of the developer. The CALIOP cloud mask algorithm utilizes a high degree of horizontal averaging to maximize sensitivity to optically thin cirrus. In the lidar-only region, above 15 km, it appears the 2C-ICE cloud mask algorithm has been tuned to be consistent with CALIOP. DARDAR was developed for application to EarthCARE joint radar–lidar observations (Ceccaldi et al., 2013), using CALIPSO-CloudSat data to develop a prototype algorithm focused on providing cloud information at a 1 km horizontal scale. Because of this the DARDAR algorithm does not do the extensive averaging used by the CALIOP algorithm and so has less sensitivity to the optically thin cirrus which is prevalent in the tropical upper troposphere. Analysis of CALIOP cloud data shows that the difference between CALIOP and DARDAR near 15 km in Fig. 19a is, qualitatively, what one would expect from limited sensitivity to thin cirrus.

For insight into the relative capabilities of CALIOP and CloudSat, Fig. 20 partitions the ice cloud occurrence frequency profiles of Fig. 19a into profiles of ice cloud occurrence frequency measured within the lidar-only, overlap, and radar-only regions of the DARDAR and 2C-ICE retrievals. The CALIOP occurrence profile of Fig. 19a is duplicated in each panel of Fig. 20, for reference. While clouds detected by CALIOP extend to 18 km, virtually no clouds are detected by CloudSat above 14 km (Fig. 20c). Lidar-only 2C-ICE cloud occurrence frequencies above 15 km agree well with L3-ICE, while lidar-only occurrence frequencies in DARDAR are significantly lower (Fig. 20a). Figure 20c shows that the CALIOP backscatter signal can be completely attenuated as high as 15 km, in the dense tops of developing deep convective clouds while, in the northern tropics, very few ice clouds are reported by CALIOP below 6 km.

Figure 21 quantifies the results shown in Fig. 20 by showing the relative number of ice cloud samples from DARDAR and from 2C-ICE which fall into the lidar-only, radar-only, or overlap regions at three specific altitudes: 8, 12, and 16 km. The corresponding tabulated results are shown in Table 6. From Fig. 21, most of the clouds at 16 km are observed by lidar only, but there are some observations falling into the overlap region and a very few observations falling into the radar-only region, likely from deep convection penetrating

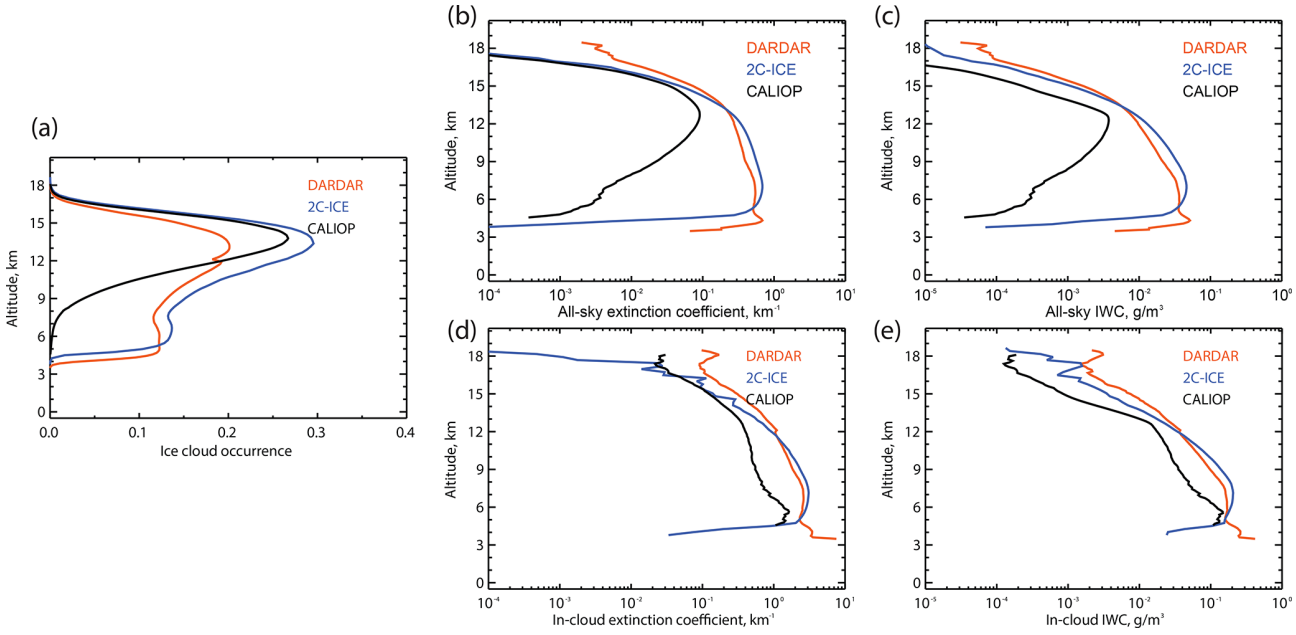

Figure 19. Comparison of ice cloud occurrence frequency **(a)**, extinction coefficient **(b, d)**, and IWC **(c, e)** profiles from L3-ICE, DARDAR, and 2C-ICE in the northern tropics (0–30° N) for July 2008. Mean all-sky extinction coefficient and IWC plotted in **(b)** and **(c)** are calculated using Eq. (6). Mean in-cloud extinction coefficient and IWC plotted in **(d)** and **(e)** are calculated using Eq. (5).

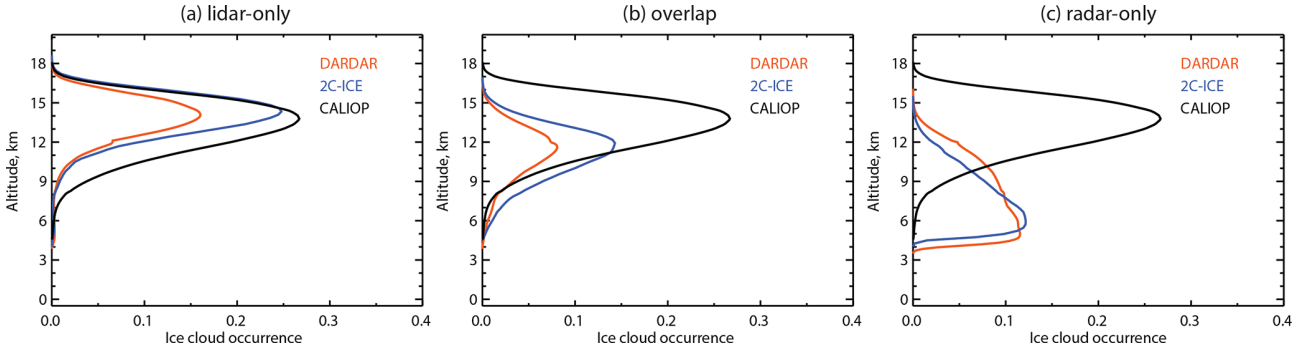

Figure 20. Profiles of cloud occurrence from DARDAR and 2C-ICE shown in Fig. 19a partitioned into lidar-only **(a)**, overlap **(b)**, and radar-only **(c)** regions. The profile of ice cloud occurrence frequency from L3-ICE is included for reference in each plot.

above 16 km. About half the data at 12 km fall into the overlap region, with a significant number of samples falling into the lidar-only and radar-only regions. At 8 km, most of the data samples are in the radar-only region with very few lidar-only samples.

Figure 22 gives additional insights into the differences between products, showing histograms of IWC at the same three altitudes near the Equator (10° S to 10° N). The histograms are computed from DARDAR and 2C-ICE in the same manner as for L3-ICE. The legend shows the mean in-cloud IWC from each product, computed using Eq. (5) with mid-bin values. All the histograms of IWC shift toward greater values of IWC as altitude decreases. At 16 km (Fig. 22a), dominated by lidar sampling (Fig. 21), the L3-ICE and 2C-ICE histograms agree quite well, while the DARDAR histogram is shifted to greater values. At 12 km (Fig. 22b) and at 8 km (Fig. 22c), L3-ICE barely reports IWC greater than 0.1 g m^{-3}, while DARDAR and 2C-ICE identify a significant number of IWC above this threshold, which results in a much smaller averaged IWC from the L3-ICE IWC histogram than that from DARDAR or 2C-ICE histogram.

7 Data availability

The Level 3 Ice Cloud product (Winker et al., 2018, https://doi.org/10.5067/CALIOP/CALIPSO/L3_ICE_CLOUD-STANDARD-V1-00) and other CALIPSO data products are freely available from the NASA Langley Research Center Atmospheric Sciences Data Center (https://asdc.larc.nasa.gov/project/CALIPSO, last access:

Table 6. Tabulated fractional ice cloud occurrence frequencies corresponding to results shown in Fig. 21.

	8 km				12 km				16 km			
	All	Lidar only	Overlap	Radar only	All	Lidar only	Overlap	Radar only	All	Lidar only	Overlap	Radar only
DARDAR	0.119	0.00300	0.0167	0.0982	0.189	0.0656	0.0741	0.0480	0.0691	0.0679	0.00105	0.0000723
2C-ICE	0.136	0.00345	0.0404	0.0921	0.255	0.0893	0.143	0.0225	0.121	0.120	0.00164	0.0000355

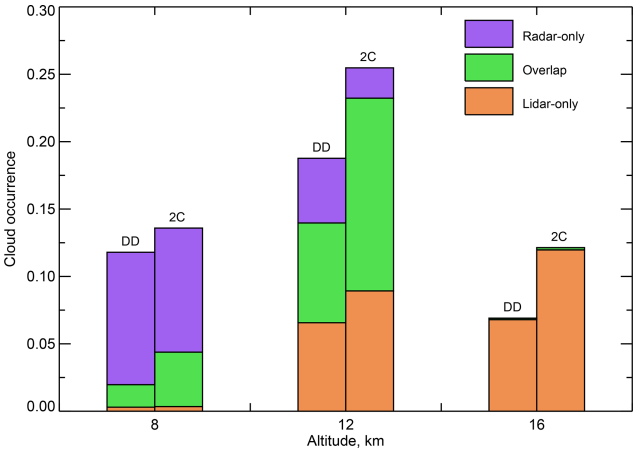

Figure 21. Fraction of ice samples at 8, 12, and 16 km, 0–30° N in July 2008, which fall into the lidar-only, overlap, and radar-only regions of DARDAR (DD) and 2C-ICE (2C).

22 May 2024) and also from the ICARE/AERIS Data and Service Center (https://www.icare.univ-lille.fr/calipso/, last access: 22 May 2024), based in Lille, France. The AERIS/ICARE Data and Services Center also hosts the DARDAR data product (https://doi.org/10.25326/449; Delanoë, 2023). The 2C-ICE product (Deng et al., 2019) is available from the CIRA data center, https://www.cloudsat.cira.colostate.edu/data-products/2c-ice.

8 Discussion and summary

That significant difficulties in the simulation of tropospheric ice clouds in climate models are due in part to a lack of high-quality global observations was noted more than 1 decade ago (Waliser et al., 2009), with perhaps the most critical need being for vertically resolved observations of ice mass, and this need persists (Duncan and Eriksson, 2018). We have described a contribution to address this need, the monthly gridded CALIPSO Level 3 Ice Cloud product (L3-ICE) derived from over 12 years of near-continuous global measurements from the CALIPSO lidar. The primary contents of the product are vertically resolved statistics on ice cloud extinction coefficients – relevant to the radiative effects of ice clouds – and profiles of cloud IWC. We have described the structure of the L3-ICE product and the methodology for its construction.

Given the unique structure of the product, we have provided several examples of how to use it. We have discussed several sources of uncertainty in the product and biases due to the limited ability of lidar to penetrate optically dense clouds. Finally, we have performed a brief comparison of L3-ICE with two frequently used radar–lidar ice cloud products, finding interesting differences at high altitudes in the lidar-only region that deserve further study.

A number of studies have pointed out large discrepancies in IWP between various satellite datasets (e.g., Waliser et al., 2009; Duncan and Eriksson, 2018). Much of the difference in mean values is due to differences in the ability of sensors to retrieve large IWP values, which can often drive monthly averages. In L3-ICE we have reported the monthly statistics as histograms rather than means and standard deviations, which provides two primary advantages. First, it allows data users to choose similar parameter ranges when comparing with ice cloud products from instruments having different detection and retrieval sensitivities. Second, the histograms are provided as sample counts to facilitate aggregation to larger space-time scales for climatological analyses or to reduce sampling uncertainties.

Our limited comparisons of L3-ICE to DARDAR and 2C-ICE illustrate the nature of differences between the products. The most obvious differences are due to the lack of observations from optically dense clouds due to reliance of 2C-ICE on lidar only. More subtle differences are seen in the lidar-only and overlap regions of DARDAR and 2C-ICE. The effective ice particle diameter, D_e, is a key parameter relating IWC to the active profile measurements. Dolinar et al. (2022) compared effective particle diameters (D_e) retrieved by 2C-ICE with the D_e used implicitly in the L3-ICE parameterization (H14), finding large differences. The parameterization of D_e in H14 was based on the best available datasets, at the time, of airborne in situ measurements. In situ ice cloud measurements provide limited sampling of ice cloud properties, as measurements are only made along aircraft trajectories, so one might think the full-cloud profile retrievals of 2C-ICE and DARDAR in the radar–lidar overlap regions would be more representative. However, the 2C-ICE and DARDAR retrievals are critically dependent on assumptions on ice particle mass–size relationships (Cazenave et al., 2019). The mass–size relationships are only partially constrained by the radar–lidar profile information, so they represent a potentially significant source of error. Therefore, de-

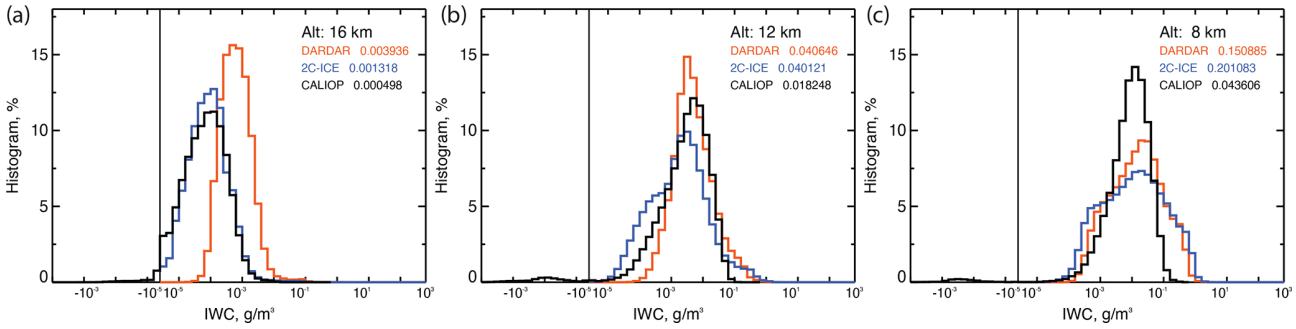

Figure 22. Normalized histograms of IWC at altitudes of **(a)** 16 km, **(b)** 12 km, and **(c)** 8 km near the Equator (10° S–10° N) in July 2008 from the L3-ICE, DARDAR, and 2C-ICE products, plotted in black, orange, and blue, respectively. Negative IWC values from L3-ICE are included on the left of the vertical solid black line.

termining whether the parameterization of H14 or the microphysical model underlying the radar–lidar retrievals provides a better retrieval of IWC is an open question at this time.

L3-ICE contains a number of different sample counts (Table 2). Some of these are necessary to compute extinction coefficients and IWC (Sect. 4) while others are provided for insight into the presence of clouds of liquid or unknown phase. The sample counts in L3-ICE are appropriate for estimating the vertical occurrence frequencies of ROI clouds but do not contain sufficient information to reliably characterize cloud occurrence for liquid and HOI clouds. Quality screening in L3-ICE is designed to ensure selection of high-quality extinction and IWC retrievals in ice clouds and is only applied to cloud layers identified as ice. N_{acc} represents the number of quality-screened samples within high-confidence ROI clouds and does not include ice layers identified as HOI, while N_{ice} includes both ROI and HOI but has not been quality screened. Therefore, neither of these sample counts is an accurate representation of ice cloud occurrence frequency. Further, sample counts for liquid clouds, N_{liq}, may be biased high due to inclusion of low-confidence layers, which represent detection artifacts rather than true cloud layers (see Fig. 2b). For all these reasons, cloud occurrences computed from the sample counts in L3-ICE may be different from other CALIOP Level 3 cloud products. But these differences are primarily due to the different objectives and strategies used in creating the cloud products and should not be considered as characterizing the uncertainties in the products.

The current L3-ICE product (V1.00) covers the time period from June 2006 through December 2018. Increasing occurrences of CALIOP low-energy laser shots have occurred since 2017. Obvious impacts on monthly Level 3 cloud statistics are seen within the South Atlantic Anomaly (SAA) by 2020, but there may be more subtle impacts earlier than that. Therefore, CALIOP data acquired from January 2017 onwards was not included in the initial release of L3-ICE. A recent analysis of data in 2017–2018 suggested that these data follow a similar trend as in years before. Therefore these data have now been released to the public. The CALIPSO team is currently developing an approach to mitigate the impact of these low-energy laser pulses on the CALIOP Level 2 data products. A future version of the L3-ICE product will be produced for the entire CALIOP mission period after this low-energy mitigation algorithm has been applied to the Level 2 data.

Appendix A: Scientific datasets (SDSs) of the CALIOP Level 3 Ice Cloud product

Longitude_Midpoint	longitude at the grid cell midpoint
Latitude_Midpoint	latitude at the grid cell midpoint
Altitude_Midpoint	altitude at the grid cell midpoint
Extinction_Coefficient_532_Bin_Boundaries	bin boundaries used for ice cloud total extinction coefficient (channel 532 nm) histogram
Ice_Water_Content_Bin_Boundaries	bin boundaries used for ice water content histogram
Pressure_Mean	mean of all pressures reported within the latitude/longitude/altitude grid cell derived from the Modern Era Retrospective-Analysis for Research (MERRA-2) reanalysis product
Pressure_Standard_Deviation	standard deviation of all pressures reported within the latitude/longitude/altitude grid cell from MERRA-2
Temperature_Mean	mean of all temperature reported within the latitude/longitude/altitude grid cell from MERRA-2
Temperature_Standard_Deviation	standard deviation of all temperature reported within the latitude/longitude/altitude grid cell from MERRA-2
Relative_Humidity_Mean	mean of all relative humidity reported within the latitude/longitude/altitude grid cell from MERRA-2
Relative_Humidity_ Standard_Deviation	standard deviation of all relative humidity reported within the latitude/longitude/altitude grid cell from MERRA-2
Tropopause_Height_Mean	mean of all tropopause height reported within the latitude/longitude grid cell from MERRA-2
Tropopause_Height_Standard_Deviation	standard deviation of all tropopause height reported within the latitude/longitude grid cell from MERRA-2
DEM_Surface_Elevation_Minimum	minimum of surface elevation for all columns reported in the latitude/longitude grid cell above local mean sea level obtained from the GTOPO30 digital elevation map (DEM).
DEM_Surface_Elevation_Maximum	maximum of surface elevation for all columns reported in the latitude/longitude grid cell from the DEM
DEM_Surface_Elevation_Median	median of surface elevation for all columns reported in the latitude/longitude grid cell from the DEM
Land_Surface_Samples	number of 5 km columns within the latitude/longitude grid cell having surface type at the middle-point lidar footprint classified as land (all surface types other than water) by the International Geosphere-Biosphere Programme (IGBP)
Water_Surface_Samples	number of 5 km columns within the latitude/longitude grid cell having surface type at the middle-point lidar footprint classified as water by the IGBP
Days_Of_Month_Observed	the days of month observed flags are bit-mapped 32-bit floats indicating which calendar days of the month CALIPSO made observations within a latitude/longitude grid cell
Extinction_Coefficient_532_Histogram	histogram of ice cloud extinction coefficient derived from the 532 nm channel in the latitude/longitude/altitude grid cell
Ice_Water_Content_Histogram	histogram of ice cloud content in the latitude/longitude/altitude grid cell

Extinction_Coefficient_532_Median	median ice cloud extinction coefficient derived from the 532 nm channel in the latitude/longitude/altitude grid cell
Ice_Water_Content_Median	median ice water content in the latitude/longitude/altitude grid cell
Lidar_Surface_Subsurface_Samples	number of lidar-detected surface or subsurface samples in the latitude/longitude/altitude grid cell
Totally_Attenuated_Samples	number of totally attenuated samples in the latitude/longitude/altitude grid cell
Cloud_Free_Samples	number of cloud-free samples in the latitude/longitude/altitude grid cell
Cloud_Samples	number of cloud samples in the latitude/longitude/altitude grid cell
Water_Cloud_Samples	number of water cloud samples in the latitude/longitude/altitude grid cell
Unknown_Cloud_Samples	number of unknown phase or not determined cloud samples in the latitude/longitude/altitude grid cell
Ice_Cloud_Samples	number of ice cloud samples in the latitude/longitude/altitude grid cell
Ice_Cloud_Rejected_Samples	number of ice cloud samples failed to pass the quality control filters in the latitude/longitude/latitude grid cell
Ice_Cloud_Accepted_Samples	number of ice cloud samples passed the quality control filters in the latitude/-longitude/latitude grid cell

Appendix B: Metadata of the CALIOP Level 3 Ice Cloud product

Product_ID	data product name
Date_Time_of_Production	date at granule production
Nominal_Year_Month	year and month when data within the Level 3 file were measured by CALIPSO
Program_Configuration	contents of the runtime program configuration file that controls the sizes of dimension used by the program, the cloud quality filter parameters, and an input file check
Number_of_Level2_Files_Analyzed	number of Level 2 granules analyzed to generate this Level 3 ice cloud file
Number_of_Bad_Profiles	number of bad 5 km profiles excluded from aggregation
List_of_Input_Files	List of included granules of Level 2 5 km Cloud Profile data product to generate this Level 3 ice cloud file

Supplement. The supplement related to this article is available online at: https://doi.org/10.5194/essd-16-2831-2024-supplement.

Author contributions. DW conceived and led the effort. XC, BM, and BG developed the product with contributions from AG, MA, and MV. XC performed the analysis. DW, XC, and MV wrote the article. All authors commented on draft versions of the article.

Competing interests. The contact author has declared that none of the authors has any competing interests.

Disclaimer. Publisher's note: Copernicus Publications remains neutral with regard to jurisdictional claims made in the text, published maps, institutional affiliations, or any other geographical representation in this paper. While Copernicus Publications makes every effort to include appropriate place names, the final responsibility lies with the authors.

Acknowledgements. We thank James Campbell, Erica Dolinar, and Andy Heymsfield for helpful discussions on the intercomparison of CALIOP retrievals with those from DARDAR and 2C-ICE. We thank the AERIS/ICARE Data and Services Center for providing access to the DARDAR data and the Cooperative Institute for Research in the Atmosphere (CIRA) for providing access to the 2C-ICE data used in this study. David Winker thanks Robert Pincus for fruitful discussions at the Max Planck Institute in Hamburg that helped shape the design of this product.

Financial support. This research was supported by the NASA Science Mission Directorate through the CALIPSO project.

Review statement. This paper was edited by Jing Wei and reviewed by two anonymous referees.

References

Avery, M. A., Ryan, R. A., Getzewich, B. J., Vaughan, M. A., Winker, D. M., Hu, Y., Garnier, A., Pelon, J., and Verhappen, C. A.: CALIOP V4 cloud thermodynamic phase assignment and the impact of near-nadir viewing angles, Atmos. Meas. Tech., 13, 4539–4563, https://doi.org/10.5194/amt-13-4539-2020, 2020.

Berry, E. and Mace, G. G.: Cloud properties and radiative effects of the Asian summer monsoon derived from A-Train data, J. Geophys. Res.-Atmos., 119, 9492–9508, https://doi.org/10.1002/2014JD021458, 2014.

Bühl, J., Alexander, S., Crewell, S., Heymsfield, A., Kalesse, H., Khain, A., Maahn, M., Van-Tricht, K., and Wendisch, M.: Ice Formation and Evolution in Clouds and Precipitation: Measurement and Modeling Challenges – Chapter 10: Remote Sensing, Meteor. Mon., 58, 10.1–10.21, https://doi.org/10.1175/AMSMONOGRAPHS-D-16-0015.1, 2017.

Cazenave, Q., Ceccaldi, M., Delanoë, J., Pelon, J., Groß, S., and Heymsfield, A.: Evolution of DARDAR-CLOUD ice cloud retrievals: new parameters and impacts on the retrieved microphysical properties, Atmos. Meas. Tech., 12, 2819–2835, https://doi.org/10.5194/amt-12-2819-2019, 2019.

Ceccaldi, M., Delanoë, J., Hogan, R. J., Pounder, N. L., Protat, A., and Pelon, J.: From CloudSat-CALIPSO to EarthCare: Evolution of the DARDAR cloud classification and its comparison to airborne radar-lidar observations, J. Geophys. Res., 118, 7962–7981, https://doi.org/10.1002/jgrd.50579, 2013.

Delanoë, J.: DARDAR CLOUD – Heymfield composite mass-size relationship, Aeris [data set], https://doi.org/10.25326/449, 2023.

Delanoë, J. and Hogan, R. J.: Combined CloudSat-CALIPSO-MODIS retrievals of the properties of ice clouds, J. Geophys. Res., 115, D00H29, https://doi.org/10.1029/2009JD012346, 2010.

Deng, M., Mace, G. G., Wang, Z., and Okamoto, H.: Tropical Composition, Cloud and Climate Coupling Experiment Validation for Cirrus Cloud Profiling Retrieval Using CloudSat Radar and CALIPSO Lidar, J. Geophys. Res., 115, D00J15, https://doi.org/10.1029/2009JD013104, 2010.

Deng, M., Mace, G. G., Wang, Z., and Berry, E.: CloudSat 2C-ICE Product Update with a New Z_e Parameterization in Lidar-only Region, J. Geophys. Res.-Atmos., 120, 12198–12208, https://doi.org/10.1002/2015JD023600, 2015.

Deng, M., Mace, G. G., and Wang, Z.: 2C-ICE PI_R05, CIRA [data set], https://www.cloudsat.cira.colostate.edu/data-products/2c-ice (last access: 21 May 2024), 2019.

Dolinar, E. K., Campbell, J. R., Marquis, J. W., Garnier, A. E., and Karpowicz, B. M.: Novel parameterization of Ice Cloud Effective Diameter from Collocated CALIOP-IIR and CloudSat Retrievals, J. Appl. Meteor. Clim. 61, 891–907, https://doi.org/10.1175/JAMC-D-21-0163.1, 2022.

Duncan, D. I. and Eriksson, P.: An update on global atmospheric ice estimates from satellite observations and reanalyses, Atmos. Chem. Phys., 18, 11205–11219, https://doi.org/10.5194/acp-18-11205-2018, 2018.

Eliasson, S., Buehler, S. A., Milz, M., Eriksson, P., and John, V. O.: Assessing observed and modelled spatial distributions of ice water path using satellite data, Atmos. Chem. Phys., 11, 375–391, https://doi.org/10.5194/acp-11-375-2011, 2011.

Garnier, A., Pelon, J., Pascal, N., Vaughan, M. A., Dubuisson, P., Yang, P., and Mitchell, D. L.: Version 4 CALIPSO Imaging Infrared Radiometer ice and liquid water cloud microphysical properties – Part II: Results over oceans, Atmos. Meas. Tech., 14, 3277–3299, https://doi.org/10.5194/amt-14-3277-2021, 2021.

Gelaro, R, McCarty, W., Suárez, M. J., Todling, R., Molod, A., Takacs, L., Randles, C. A., Darmenov, A., Bosilovich, M. G., Reichle, R., Wargan, K., Coy, L., Cullather, R., Draper, C., Akella, S., Buchard, V., Conaty, A., da Silva, A. M., Gu, W., Kim, G., Koster, R., Lucchesi, R., Merkova, D., Nielsen, J. E., Partyka, G., Pawson, S., Putman, W., Rienecker, M., Schubert, S. D., Sienkiewicz, M., and Zhao, B.: The Modern-Era Retrospective Analysis for Research and Applications, Version 2 (MERRA-2), J. Climate, 30, 5419–5454, https://doi.org/10.1175/JCLI-D-16-0758.1, 2017.

Getzewich, B. J., Vaughan, M. A., Hunt, W. H., Avery, M. A., Powell, K. A., Tackett, J. L., Winker, D. M., Kar, J., Lee, K.-P., and Toth, T. D.: CALIPSO lidar calibration at 532 nm: version 4 daytime algorithm, Atmos. Meas. Tech., 11, 6309–6326, https://doi.org/10.5194/amt-11-6309-2018, 2018.

Haladay, T. and Stephens, G.: Characteristics of Tropical Thin Cirrus Clouds Deduced from Joint CloudSat and CALIPSO Observations, J. Geophys. Res., 114, D00A25, https://doi.org/10.1029/2008JD010675, 2009.

Heymsfield, A., Winker, D., Avery, M., Vaughan, M., Diskin, G., Deng, M., Mitev, V., and Matthey, R.: Relationships between Ice Water Content and Volume Extinction Coefficient from In Situ Observations for Temperatures from 0° to −86 °C: Implications for Spaceborne Lidar Retrievals, J. Appl. Meteor. Climatol., 53, 479–505, https://doi.org/10.1175/JAMC-D-13-087.1, 2014.

Hong, Y., Liu, G., and Li, J.-L. F.: Assessing the Radiative Effects of Global Ice Clouds Based on CloudSat and CALIPSO Measurements, J. Climate, 29, 7651–7674, https://doi.org/10.1175/JCLI-D-15-0799.1, 2016.

Hu, Y.: Depolarization ratio–effective lidar ratio relation: Theoretical basis for space lidar cloud phase discrimination, Geophys. Res. Lett., 34, L11812, https://doi.org/10.1029/2007GL029584, 2007.

Hunt, W. H., Winker, D. M., Vaughan, M. A., Powell, K. A., Lucker, P. L., and Weimer, C.: CALIPSO Lidar Description and Performance Assessment, J. Atmos. Ocean. Tech., 26, 1214–1228, https://doi.org/10.1175/2009JTECHA1223.1, 2009.

Kar, J., Vaughan, M. A., Lee, K.-P., Tackett, J. L., Avery, M. A., Garnier, A., Getzewich, B. J., Hunt, W. H., Josset, D., Liu, Z., Lucker, P. L., Magill, B., Omar, A. H., Pelon, J., Rogers, R. R., Toth, T. D., Trepte, C. R., Vernier, J.-P., Winker, D. M., and Young, S. A.: CALIPSO lidar calibration at 532 nm: version 4 nighttime algorithm, Atmos. Meas. Tech., 11, 1459–1479, https://doi.org/10.5194/amt-11-1459-2018, 2018.

Key, J. R.: Estimating the Area Fraction of Geophysical Fields from Measurements Along a Transect, IEEE Trans. Geosci. Remote, 31, 1099–1102, https://doi.org/10.1109/36.263782, 1993.

Kotarba, A. Z.: Errors in global cloud climatology due to transect sampling with the CALIPSO satellite lidar mission, Atmos. Res., 279, 106379, https://doi.org/10.1016/j.atmosres.2022.106379, 2022.

Kotarba, A. Z. and Solecki, M.: Uncertainty Assessment of the Vertically-Resolved Cloud Amount for Joint CloudSat–CALIPSO Radar–Lidar Observations, Remote Sens., 13, 807, https://doi.org/10.3390/rs13040807, 2021.

Li, J.-L. F., Waliser, D. E., Stephens, G., and Lee, S.: Characterizing and Understanding Cloud Ice and Radiation Budget Biases in Global Climate Models and Reanalysis, Meteor. Mon., 56, 13.01–13.20, https://doi.org/10.1175/AMSMONOGRAPHS-D-15-0007.1, 2016.

Liu, Z., Kar, J., Zeng, S., Tackett, J., Vaughan, M., Avery, M., Pelon, J., Getzewich, B., Lee, K.-P., Magill, B., Omar, A., Lucker, P., Trepte, C., and Winker, D.: Discriminating between clouds and aerosols in the CALIOP version 4.1 data products, Atmos. Meas. Tech., 12, 703–734, https://doi.org/10.5194/amt-12-703-2019, 2019.

Mace, G., Zhang, Q., Vaughan, M., Marchand, R., Stephens, G., Trepte, C., and Winker, D.: A Description of Hydrometeor Layer Occurrence Statistics Derived from the First Year of Merged Cloudsat and CALIPSO Data, J. Geophys. Res., 114, D00A26, https://doi.org/10.1029/2007JD009755, 2009.

Mioche, G., Josset, D., Gayet, J.-F., Pelon, J., Garnier, A., Minikin, A., and Schwarzenboeck, A.: Validation of the CALIPSO/-CALIOP extinction coefficients from in situ observations in mid-latitude cirrus clouds during CIRCLE-2 experiment, J. Geophys. Res., 115, D00H25, https://doi.org/10.1029/2009JD012376, 2010.

Murtagh, D. Frisk, U., Merino, F., Ridal, M., Jonsson, A., Stegman, J., Witt, G., Eriksson, P., Jiménez, C., Megie, G., de la Noë, J., Ricaud, P., Baron, P., Pardo, J. R., Hauchcorne, A., Llewellyn, E. J., Degenstein, D. A., Gattinger, R. L., Lloyd, N. D., Evans, W. F. J., McDade, I. C., Haley, C. S., Sioris, C., von Savigny, C., Solheim, B. H., McConnell, J. C., Strong, K., Richardson, E. H., Leppelmeier, G. W., Kyrölä, E., Auvinen, H., and Oikarinen, L.: An overview of the Odin atmospheric mission, Can. J. Phys., 80, 309–318, https://doi.org/10.1139/p01-157, 2002.

NASA JPL: NASA Shuttle Radar Topography Mission Global 1 arc second, NASA EOSDIS Land Processes DAAC [data set], https://doi.org/10.5067/MEaSUREs/SRTM/SRTMGL1.003 (last access: 23 February 2023), 2013.

Noël, V. and Sassen, K.: Study of planar ice crystal orientations in ice clouds from scanning polarization lidar observations, J. Appl. Meteor, 44, 643–664, https://doi.org/10.1175/JAM2223.1, 2005.

Noel, V., Chepfer, H., Chiriaco, M., and Yorks, J.: The diurnal cycle of cloud profiles over land and ocean between 51° S and 51° N, seen by the CATS spaceborne lidar from the International Space Station, Atmos. Chem. Phys., 18, 9457–9473, https://doi.org/10.5194/acp-18-9457-2018, 2018.

Powell, K. A., Hostetler, C. A., Liu, Z., Vaughan, M. A., Kuehn, R. E., Hunt, W. H., Lee, K., Trepte, C. R., Rogers, R. R., Young, S. A., and Winker, D. M.: CALIPSO Lidar Calibration Algorithms: Part I – Nighttime 532 nm Parallel Channel and 532 nm Perpendicular Channel, J. Atmos. Ocean. Tech., 26, 2015–2033, https://doi.org/10.1175/2009JTECHA1242.1, 2009.

Pitts, M. C., Poole, L. R., and Gonzalez, R.: Polar stratospheric cloud climatology based on CALIPSO spaceborne lidar measurements from 2006 to 2017, Atmos. Chem. Phys., 18, 10881–10913, https://doi.org/10.5194/acp-18-10881-2018, 2018.

Sassen, K.: Ice crystal habit discrimination with the optical backscatter depolarization technique, J. Appl. Meteor., 16, 425–431, 1977.

Sassen, K., Wang, Z., and Liu, D.: Cirrus clouds and deep convection in the tropics: Insights from CALIPSO and CloudSat, J. Geophys. Res., 114, D00H06, https://doi.org/10.1029/2009JD011916, 2009.

Silber, I., Fridlind, A. M., Verlinde, J., Ackerman, A. S., Cesana, G. V., and Knopf, D. A.: The prevalence of precipitation from polar supercooled clouds, Atmos. Chem. Phys., 21, 3949–3971, https://doi.org/10.5194/acp-21-3949-2021, 2021.

Stephens, G. L., Vane, D. G., Boain, R. J., Mace, G. G., Sassen, K., Wang, Z., Illingworth, A. J., O'Connor, E. J., Rossow, W. B., Durden, S. L., Miller, S. D., Austin, R. T., Benedetti, A., Mitrescu, C., and the CloudSat Team: The CloudSat Mission and the A-Train, B. Am. Meteorol. Soc., 1771-1790, https://doi.org/10.1175/BAMS-83-12-1771, 2002.

Tackett, J. L., Winker, D. M., Getzewich, B. J., Vaughan, M. A., Young, S. A., and Kar, J.: CALIPSO lidar level 3 aerosol pro-

file product: version 3 algorithm design, Atmos. Meas. Tech., 11, 4129–4152, https://doi.org/10.5194/amt-11-4129-2018, 2018.

Tackett, J., Ryan, R., Vaughan, M, Garnier, A., Getzewich, B., Winker, D., and Trepte, C.: Mitigation Strategy for the Impact of Low Energy Laser Pulses in CALIOP Calibration and Level 2 Retrievals, Proceedings of the 30th International Laser Radar Conference, 617–623, https://doi.org/10.1007/978-3-031-37818-8_79, 2023.

Tanelli, S., Dobrowalski, G., Lebsock, M., Durden, S. L., Partain, P., Reinke, D., and Reinke, D: CloudSat's Cloud Profiling Radar: Status, Performance, and latest data product changes, CALIPSO-CloudSat Science Team Meeting, 3–5 November 2014, Alexandria VA USA, 2014.

Vaughan, M. A., Winker, D. M., and Powell, K. A.: CALIOP Algorithm Theoretical Basis Document, Part 2: Feature Detection and Layer Properties Algorithms, PC-SCI-202.01, https://www-calipso.larc.nasa.gov/resources/project_documentation.php (last access: 3 April 2023), 2005.

Vaughan, M., Powell, K., Kuehn, R., Young, S., Winker, D., Hostetler, C., Hunt, W., Liu, Z., McGill, M., and Getzewich, B.: Fully Automated Detection of Cloud and Aerosol Layers in the CALIPSO Lidar Measurements, J. Atmos. Ocean. Tech., 26, 2034–2050, https://doi.org/10.1175/2009JTECHA1228.1, 2009.

Vaughan, M., Garnier, A., Josset, D., Avery, M., Lee, K.-P., Liu, Z., Hunt, W., Pelon, J., Hu, Y., Burton, S., Hair, J., Tackett, J. L., Getzewich, B., Kar, J., and Rodier, S.: CALIPSO lidar calibration at 1064 nm: version 4 algorithm, Atmos. Meas. Tech., 12, 51–82, https://doi.org/10.5194/amt-12-51-2019, 2019.

Vaughan, M., Pitts, M., Trepte, C., Winker, D., Detweiler, P., Garnier, A., Getzewich, B., Hunt, W., Lambeth, J., Lee, K.-P., Lucker, P., Murray, T., Rodier, S., Tremas, T., Bazureau, A., and Pelon, J.: Cloud-Aerosol LIDAR Infrared Pathfinder Satellite Observations (CALIPSO) data management system data products catalog, Release 4.95, NASA Langley Research Center Document PC-SCI-503, 277 pp., https://www-calipso.larc.nasa.gov/products/CALIPSO_DPC_Rev4x95.pdf (last access: 10 July 2023), 2023.

Waliser, D. E., Li, J.-L. F., Woods, C. P., Austin, R. T., Bacmeister, J., Chern, J., Del Genio, A., Jiang, J. H., Kuang, Z., Meng, H., Minnis, P., Platnick, S., Rossow, W. B., Stephens, G. L., Sun-Mack, S., Tao, W.-K., Tompkins, A. M., Vane, D. G., Walker, C., and Wu, D.: Cloud ice: A climate model challenge with signs and expectations of progress, J. Geophys. Res., 114, D00A21, https://doi.org/10.1029/2008JD010015, 2009.

Waters, J. W., Froidevaux, L., Harwood, R. S., Jarnot, R. F., Pickett, H. M., Read, W. G., Siegel, P. H., Cofield, R. E., Filipiak, M. J., Flower, D. A., Holden, J. R., Lau, G. K., Livesey, N. J., Manney, G. L., Pumphrey, H. C., Santee, M. L., Wu, D. L., Cuddy, D. T., Lay, R. R., Loo, M. S., Perun, V. S., Schwartz, M. J., Stek, P. C., Thurstans, R. P., Boyles, M. A., Chandra, K. M., Chavez, M. C., Chen, G.-S., Chudasama, B. V., Dodge, R., Fuller, R. A., Girard, M. A., Jiang, J. H., Jiang, Y., Knosp, B. W., LaBelle, R. C., Lam, J. C., Lee, K. A., Miller, D., Oswald, J. E., Patel, N. C., Pukala, D. M., Quintero, O., Scaff, D. M., van Snyder, W., Tope, M. C., Wagner, P. A., and Walch, M. J.: The Earth Observing System Microwave Limb Sounder (EOS MLS) on the Aura satellite, IEEE Trans. Geosci. Remote Sens., 44, 1075–1092, https://doi.org/10.1109/TGRS.2006.873771, 2006.

Winker, D. M., Vaughan, M. A., Omar, A. H., Hu, Y., Powell, K. A., Liu, Z., Hunt, W. H., and Young, S. A.: Overview of the CALIPSO Mission and CALIOP Data Processing Algorithms, J. Atmos. Ocean. Tech., 26, 2310–2323, https://doi.org/10.1175/2009JTECHA1281.1, 2009.

Winker, D. M., Pelon, J., Coakley Jr., J. A., Ackerman, S. A., Charlson, R. J., Colarco, P. R., Flamant, P., Fu, Q., Hoff, R. M., Kittaka, C., Kubar, T. L., Le Treut, H., McCormick, M. P., Megie, G., Poole, L., Powell, K., Trepte, C., Vaughan, M. A., and Wielicki, B. A.: The CALIPSO mission: A Global 3D view of aerosols and clouds, B. Am. Meteorol. Soc., 91, 1211–1229, https://doi.org/10.1175/2010BAMS3009.1, 2010.

Winker, D. M., Tackett, J. L., Getzewich, B. J., Liu, Z., Vaughan, M. A., and Rogers, R. R.: The global 3-D distribution of tropospheric aerosols as characterized by CALIOP, Atmos. Chem. Phys., 13, 3345–3361, https://doi.org/10.5194/acp-13-3345-2013, 2013.

Winker, D., Chepfer, H., Noël, V., and Cai, X.: Observational Constraints on Cloud Feedbacks: The Role of Active Satellite Sensors, Surv. Geophys., 38, 1483–1508, https://doi.org/10.1007/s10712-017-9452-0, 2017.

Winker, D. M., Cai, X., McGill, B., Getzewich, B., Vaughan, M., Garnier, A., and Avery, M.: CALIPSO Level 3 Ice Cloud Product, Atmospheric Sciences Data Center (ASDC) [data set], https://doi.org/10.5067/CALIOP/CALIPSO/L3_ICE_CLOUD-STANDARD-V1-00, 2018.

Wu, D. L., Jiang, J. H., Read, W. G., Austin, R. T., Davis, C. P., Lambert, A., Stephens, G. L., Vane, D. G., and Waters, J. W.: Validation of the Aura MLS cloud ice water content measurements, J. Geophys. Res., 113, D15S10, https://doi.org/10.1029/2007JD008931, 2008.

Wu. D., Austin, R. T., Deng, M., Durden, S. L., Heymsfield, A. J., Jiang, J. H., Lambert, A., Li, J.-L., Livesey, N. J., McFarquhar, G. M., Pittman, J. V., Stephens, G. L., Tanelli, S., Vane, D. G., and Waliser, D. E.: Comparisons of global cloud ice from MLS, CloudSat, and correlative data sets, J. Geophys. Res., 114, D00A24, https://doi.org/10.1029/2008JD009946, 2009.

Young, S. A. and Vaughan, M. A.: The retrieval of profiles of particulate extinction from Cloud Aerosol Lidar Infrared Pathfinder Satellite Observations (CALIPSO) data: Algorithm description, J. Atmos. Ocean. Tech., 26, 1105–1119, https://doi.org/10.1175/2008JTECHA1221.1, 2009.

Young, S. A., Vaughan, M. A., Kuehn, R. E., and Winker, D. M.: The Retrieval of Profiles of Particulate Extinction from Cloud-Aerosol Lidar Infrared Pathfinder Satellite Observations (CALIPSO) Data: Uncertainty and Error Sensitivity Analyses, J. Atmos. Ocean. Tech., 30, 395–428, https://doi.org/10.1175/JTECH-D-12-00046.1, 2013.

Young, S. A., Vaughan, M. A., Garnier, A., Tackett, J. L., Lambeth, J. D., and Powell, K. A.: Extinction and optical depth retrievals for CALIPSO's Version 4 data release, Atmos. Meas. Tech., 11, 5701–5727, https://doi.org/10.5194/amt-11-5701-2018, 2018.

Zhang, D., Wang, Z., and Liu, D.: A global view of midlevel liquid-layer topped stratiform cloud distribution and phase partition from CALIPSO and CloudSat measurements, J. Geophys. Res., 115, D00H13, https://doi.org/10.1029/2009JD012143, 2010.